

Spin Orbit Misalignments in Tertiary-Induced Black-Hole Binary Mergers: Theoretical Analysis

Yubo Su, Dong Lai, and Bin Liu

*Cornell Center for Astrophysics and Planetary Science,
Department of Astronomy, Cornell University, Ithaca, NY 14853, USA**

(Dated: October 20, 2020)

Black-hole (BH) binary mergers driven by gravitational perturbations of tertiary companions constitute an important class of dynamical formation channels for merging BH binaries detected by LIGO/VIRGO. Recent works have examined numerically the combined orbital and spin dynamics of BH binaries that undergo large Lidov-Kozai (LK) eccentricity oscillations due to the influence of a highly inclined tertiary companion and merge via gravitational wave radiation. However, the extreme eccentricity variations make such systems difficult to characterize analytically. In this paper, we develop an analytical formalism for understanding the spin dynamics of binary BHs undergoing LK-induced mergers. We show that, under certain conditions, the eccentricity oscillations of the binary can be averaged over to determine the long-term behavior of the BH spin in a smooth way. In particular, we demonstrate that the final spin-orbit misalignment angle θ_{s1} when the inner binary gravitationally decouples from the tertiary companion is often related to the binary’s primordial spin orientation through an approximate adiabatic invariant. Our theory explains the “90° attractor” (found in recent numerical studies) for the evolution of θ_{s1} when the initial BH spin is aligned with the orbital axis and the octupole LK effects are negligible—such a “90° attractor” would lead to a small binary effective spin parameter $\chi_{\text{eff}} \sim 0$ even for large intrinsic BH spins. We calculate the deviation from adiabaticity in closed form as a function of initial conditions. We also place accurate constraints on when this adiabatic invariant breaks down due to resonant spin-orbit interactions. We consider both stellar-mass and supermassive BH tertiary companions, and provide simple prescriptions for determining analytically the final spin-orbit misalignment angles of the merging BH binaries.

I. INTRODUCTION

As LIGO/VIRGO continues to detect mergers of black hole (BH) binaries [e.g. 1, 2], it is increasingly important to systematically study various formation channels of BH binaries and their observable signatures. The canonical channel consists of isolated binary evolution, in which mass transfer and friction in the common envelope phase cause the binary orbit to decay sufficiently that it subsequently merges via emission of gravitational waves (GW) within a Hubble time [e.g. 3–10]. BH binaries formed via isolated binary evolution are generally expected to have small misalignment between the BH spin axis and the orbital angular momentum axis [11, 12]. On the other hand, various flavors of dynamical formation channels of BH binaries have also been studied. These involve either strong gravitational scatterings in dense clusters [e.g. 13–23] or more gentle “tertiary-induced mergers” [e.g. 24–33]. The dynamical formation channels generally produce BH binaries with misaligned spins **with respect to the orbital axes**.

GW observations of binary inspirals can put constraints on BH masses and spins. Typically, spin constraints come in the form of two dimensionless mass-weighted combinations of the component BH spins: (i) the aligned spin parameter

$$\chi_{\text{eff}} \equiv \frac{m_1 \chi_1 \cos \theta_{s1} + m_2 \chi_2 \cos \theta_{s2}}{m_1 + m_2}, \quad (1)$$

where $m_{1,2}$ are the masses of the BHs, θ_{s1} is the angle between the i -th spin and the binary orbital angular momentum axis, and $\chi_i \equiv cS_i/(Gm_i^2)$ is the dimensionless Kerr spin parameter;

and (ii) the perpendicular spin parameter [34]

$$\chi_p \equiv \max \left\{ \chi_1 \sin \theta_{s1}, \frac{q(4q+3)}{4+3q} \chi_2 \sin \theta_{s2} \right\}, \quad (2)$$

where $q \equiv m_2/m_1$ and $m_1 \geq m_2$. The systems detected in the **first and second observing runs (O1 and O2) of LIGO/VIRGO** have $\chi_{\text{eff}} \sim 0$ (but see [35, 36] for exceptions). In the **third observing run (O3) of LIGO/VIRGO**, two events exhibit substantial spin-orbit misalignment. In GW190412 [37], the two BH component masses are $29^{+5.0}_{-5.3} M_\odot$ and $8.4^{+1.7}_{-1.0} M_\odot$. The primary (more massive) BH is inferred to have $\chi_1 = 0.43^{+0.16}_{-0.26}$, and the effective spin parameter of the binary is constrained to be $\chi_{\text{eff}} = 0.25^{+0.09}_{-0.11}$, indicating a non-negligible spin-orbit misalignment angle. In GW190521 [38], the two component BHs have masses of $85^{+21}_{-14} M_\odot$ and $66^{+17}_{-18} M_\odot$ and spins of $\chi_1 = 0.69^{+0.27}_{-0.62}$ and $\chi_2 = 0.72^{+0.24}_{-0.64}$. The binary’s aligned spin is $\chi_{\text{eff}} = 0.08^{+0.27}_{-0.36}$ while the perpendicular spin is $\chi_p = 0.68^{+0.25}_{-0.37}$, again suggesting significant spin-orbit misalignments.

Liu and Lai [30, 31, hereafter LL17, LL18], and Liu *et al.* [39] carried out a systematic study of binary BH mergers in the presence of a tertiary companion. LL17 pointed out the important effect of spin-orbit coupling (de-Sitter precession) in determining the final spin-orbit misalignment angles of BH binaries in triple systems. They considered binaries with sufficiently compact orbits (so that mergers are possible even without a tertiary) and showed that the combination of LK oscillations (induced by a modestly inclined tertiary) and spin-orbit coupling gives rise to a broad range of final spin-orbit **misalignments** in the merging binary BHs. We call these mergers *LK-enhanced mergers*. LL18 considered the most interesting case of *LK-induced mergers*, in which an initially wide BH binary (too wide to merge in isolation) is pushed to extreme

* yubosu@astro.cornell.edu

eccentricities (close to unity) by a highly inclined tertiary and merges within a few Gyrs. LL18 examined a wide range of orbital and spin evolution behaviors and found that LK-induced mergers can sometimes yield a “90° attractor”: when the BH spin is initially aligned with the inner binary angular momentum axis ($\theta_{\text{sl},0} = 0$), it evolves towards a perpendicular state ($\theta_{\text{sl},f} \simeq 90^\circ$) near merger. Qualitatively, they found that the attractor exists when the LK-induced orbital decay is sufficiently “gentle” and the octupole effect is unimportant. Fig. 1 gives an example of a system evolving towards this attractor, where θ_{sl} converges to $\simeq 90^\circ$ at late times in the bottom right panel. Fig. 2 shows how $\theta_{\text{sl},f}$ varies when the initial inclination of the tertiary orbit I_0 (relative to the inner orbit) is varied. Note that for rapid mergers (when I_0 is close to 90°), the attractor does not exist; as I_0 deviates more from 90° , the merger time increases and $\theta_{\text{sl},f}$ is close to 90° . This 90° attractor gives rise to a peak around $\chi_{\text{eff}} = 0$ in the final χ_{eff} distribution in tertiary-induced mergers [LL18; 39]. This peak was also found in the population studies of Antonini *et al.* [40].

The physical origin of this 90° attractor and under what conditions it can be achieved are not well understood. LL18 proposed an explanation based on analogy with an adiabatic invariant in systems where the inner binary remains circular throughout the inspiral (LL17). However, the validity of this analogy is **hard to justify**, as significant eccentricity excitation is a necessary ingredient in LK-induced mergers. In addition, the LK-enhanced mergers considered in LL17 show no 90° attractor even though the orbital evolution is slow and regular.

In this paper, we **present an analytic theory to explain** the 90° attractor and **to characterize** its regime of validity. In Sections II and III, we set up the relevant equations of motion for the orbital and spin evolution of the system. **To simplify the theoretical analysis, we initially consider the cases where the tertiary mass is much larger than the binary mass.** In Sections IV and V, we develop an analytic understanding of the spin evolution. In Section VI, we generalize our results to stellar-mass tertiary companions. We discuss and conclude in Section VII.

II. LK-INDUCED MERGERS: ORBITAL EVOLUTION

In this section we summarize the key features and relevant equations for LK-induced mergers to be used for our analysis in later sections. Consider a black hole (BH) binary with masses m_1 and m_2 having total mass m_{12} , reduced mass $\mu = m_1 m_2 / m_{12}$, semimajor axis a and eccentricity e . This inner binary orbits around a tertiary with mass m_3 , semimajor axis a_{out} and eccentricity e_{out} in a hierarchical configuration ($a_{\text{out}} \gg a$). Unless explicitly stated, we assume $m_3 \gg m_1, m_2$ (e.g. the tertiary can be a supermassive black hole, or SMBH), although our analysis can be easily generalized to comparable masses (see Section VI). We denote the orbital angular momentum of the inner binary by $\mathbf{L} \equiv L\hat{\mathbf{L}}$ and the angular momentum of the outer binary by $\mathbf{L}_{\text{out}} \equiv L_{\text{out}}\hat{\mathbf{L}}_{\text{out}}$. Since $L_{\text{out}} \gg L$, we take \mathbf{L}_{out} to be fixed.

The equations of motion governing the orbital elements a , e , φ , I , ω (where φ , I , ω are the longitude of the ascending

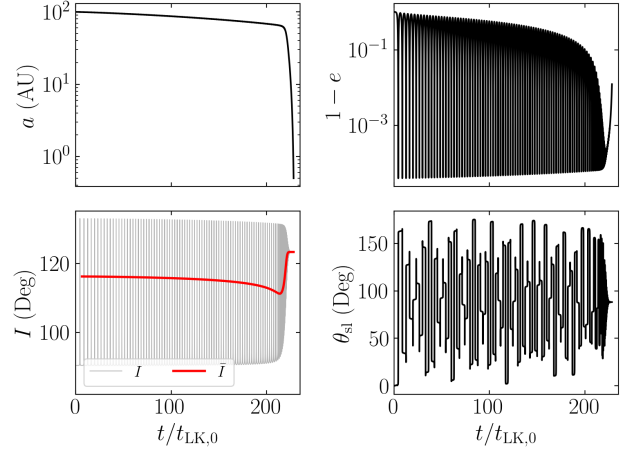


FIG. 1. An example of the “90° spin attractor” in LK-induced BH binary mergers. The four panes show the time evolution of the binary semi-major axis a , eccentricity e , inclination I [the red line denotes the averaged \bar{I} given by Eq. (29)], and spin-orbit misalignment angle θ_{sl} . The unit of time $t_{\text{LK},0}$ is the LK timescale [Eq. (9)] evaluated for the initial conditions. The inner binary has $m_1 = 30M_\odot$, $m_2 = 20M_\odot$, and initial $a_0 = 100$ AU, $e_0 = 0.001$, $I_0 = 90.35^\circ$ (with respect to the outer binary), and $\theta_{\text{sl},0} = 0$. The tertiary has $a_{\text{out}} = 2.2$ pc, $e_{\text{out}} = 0$, and $m_3 = 3 \times 10^7 M_\odot$ (The result depends only on $m_3/\tilde{a}_{\text{out}}^3$, provided that $L_{\text{out}} \gg L$). It can be seen that θ_{sl} evolves to $\sim 90^\circ$ as a decays to smaller values, and we stop the simulation when $a = 0.5$ AU as the LK oscillation “freezes” and θ_{sl} has converged to a constant value.

node, inclination, and argument of periapsis respectively) of the inner binary are

$$\frac{da}{dt} = \left(\frac{da}{dt} \right)_{\text{GW}}, \quad (3)$$

$$\frac{de}{dt} = \frac{15}{8t_{\text{LK}}} e j(e) \sin 2\omega \sin^2 I + \left(\frac{de}{dt} \right)_{\text{GW}}, \quad (4)$$

$$\frac{d\varphi}{dt} = \frac{3}{4t_{\text{LK}}} \frac{\cos I (5e^2 \cos^2 \omega - 4e^2 - 1)}{j(e)}, \quad (5)$$

$$\frac{dI}{dt} = -\frac{15}{16t_{\text{LK}}} \frac{e^2 \sin 2\omega \sin 2I}{j(e)}, \quad (6)$$

$$\frac{d\omega}{dt} = \frac{3}{4t_{\text{LK}}} \frac{2j^2(e) + 5 \sin^2 \omega (e^2 - \sin^2 I)}{j(e)} + \Omega_{\text{GR}}, \quad (7)$$

where we have defined

$$j(e) = \sqrt{1 - e^2}, \quad (8)$$

$$t_{\text{LK}}^{-1} \equiv n \left(\frac{m_3}{m_{12}} \right) \left(\frac{a}{\tilde{a}_{\text{out}}} \right)^3, \quad (9)$$

with $n \equiv \sqrt{Gm_{12}/a^3}$ the mean motion of the inner binary, and $\tilde{a}_{\text{out}} = a_{\text{out}} \sqrt{1 - e_{\text{out}}^2}$. The GR-induced apsidal precession of the inner binary is given by

$$\Omega_{\text{GR}}(e) = \frac{3Gnm_{12}}{c^2 a j^2(e)}. \quad (10)$$

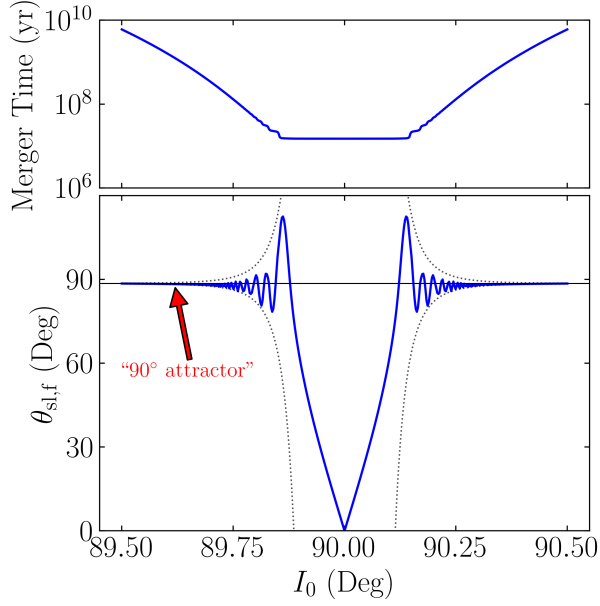


FIG. 2. The merger time and the final spin-orbit misalignment angle $\theta_{\text{sl},f}$ as a function of the initial inclination I_0 for LK-induced mergers. The other parameters are the same as those in Fig. 1. For I_0 somewhat far away from 90° , the resulting $\theta_{\text{sl},f}$ are all quite near 90° . In the lower panel, the horizontal black solid line shows the predicted $\theta_{\text{sl},f}$ if $\bar{\theta}_e$ is conserved, i.e. Eq. (57), and the black dashed line shows Eq. (61), which provides an estimate for the deviation from the 90° attractor.

The dissipative terms due to gravitational radiation are

$$\left(\frac{da}{dt}\right)_{\text{GW}} = -\frac{a}{t_{\text{GW}}(e)}, \quad (11)$$

$$\left(\frac{de}{dt}\right)_{\text{GW}} = -\frac{304}{15} \frac{G^3 \mu m_{12}^2}{c^5 a^4} \frac{1}{j^{5/2}(e)} \left(1 + \frac{121}{304} e^2\right), \quad (12)$$

where

$$t_{\text{GW}}^{-1}(e) \equiv \frac{64}{5} \frac{G^3 \mu m_{12}^2}{c^5 a^4} \frac{1}{j^{7/2}(e)} \left(1 + \frac{73}{24} e^2 + \frac{37}{96} e^4\right). \quad (13)$$

Equations (4–7) include only the effects of quadrupole perturbations from m_3 on the binary. The octupole effects depend on the parameter

$$\epsilon_{\text{oct}} = \frac{m_1 - m_2}{m_{12}} \frac{a e_{\text{out}}}{a_{\text{out}}(1 - e_{\text{out}}^2)}, \quad (14)$$

[see 41]. Throughout this paper, we consider $a_{\text{out}} \gg a$ and $e_{\text{out}} = 0$, so that the octupole effects are neglected.

In Fig. 1, we provide an example of an LK-induced merger for our fiducial parameters (described in the figure caption). The inner binary initially decays slowly as its eccentricity undergoes LK oscillations, with a nearly constant maximum eccentricity close to unity. Then, as a decreases and the minimum eccentricity within each LK cycle increases, the orbital

decay of the inner binary accelerates. As apsidal precession further suppresses eccentricity oscillations, the eccentricity rapidly decays. We terminate the simulation at $a = 0.5$ AU as the spin-orbit misalignment angle θ_{sl} has reached its final value, even though the binary still has non-negligible eccentricity. We refer to the example depicted in Fig. 1 as the fiducial example, and much of our analysis in later sections will be based on this example unless otherwise noted. Also note that the parameters of Fig. 1 give the same t_{LK} as Fig. 4 of LL18.

We next discuss the key analytical properties of the orbital evolution.

A. Analytical Results Without GW Radiation

First, neglecting the GW radiation terms, the system admits two conservation laws, the “Kozai constant” and energy conservation,

$$j(e) \cos I = \text{const}, \quad (15)$$

$$\frac{3}{8} \left[2e^2 + j^2(e) \cos^2 I - 5e^2 \sin^2 I \sin^2 \omega \right] + \frac{\epsilon_{\text{GR}}}{j(e)} = \text{const}, \quad (16)$$

(see [42] and LL18 for more general expressions when L_{out} is comparable to L), where

$$\epsilon_{\text{GR}} \equiv (\Omega_{\text{GR}} t_{\text{LK}})_{e=0} = \frac{3Gm_{12}^2 \tilde{a}_{\text{out}}^3}{c^2 m_3 a^4}. \quad (17)$$

The conservation laws can be combined to obtain the maximum eccentricity e_{max} as a function of the initial I_0 (and initial $e_0 \ll 1$). The largest value of e_{max} occurs at $I_0 = 90^\circ$ and is given by

$$j(e_{\text{max}})_{I_0=90^\circ} = (8/9) \epsilon_{\text{GR}}. \quad (18)$$

Eccentricity excitation then requires $\epsilon_{\text{GR}} < 9/8$. Our fiducial examples in Figs. 1 and 2 satisfy $\epsilon_{\text{GR}} \ll 1$ at $a = a_0$, leading to $e_{\text{max}} \sim 1$ within a narrow inclination window around $I_0 = 90^\circ$.

Eqs. (15) and (16) imply that e is a function of $\sin^2 \omega$ alone [see 43, 44, for the exact form], so an eccentricity maximum occurs every half period of ω . We define the period and angular frequency of eccentricity oscillation via

$$\pi = \int_0^{P_{\text{LK}}} \frac{d\omega}{dt} dt, \quad \Omega_{\text{LK}} \equiv \frac{2\pi}{P_{\text{LK}}}. \quad (19)$$

In LK cycles, the inner binary oscillates between the eccentricity minimum e_{min} and maximum e_{max} . The oscillation is “uneven”: when $e_{\text{min}} \ll e_{\text{max}}$, the binary spends a fraction $\sim j(e_{\text{max}})$ of the LK cycle, or time $\Delta t \sim t_{\text{LK}} j(e_{\text{max}})$, near $e \simeq e_{\text{max}}$ [see Eq. (7)].

B. Behavior with GW Radiation

Including the effect of GW radiation, orbital decay predominantly occurs at $e \simeq e_{\text{max}}$ with the timescale of $t_{\text{GW}}(e_{\text{max}})$

[see Eq. (13)]. On the other hand, Eq. (7) implies that, when $\epsilon_{\text{GR}} \ll 1$, the binary spends only a small fraction ($\sim j(e_{\text{max}})$) of the time near $e \simeq e_{\text{max}}$. Thus, we expect two qualitatively different merger behaviors:

- “Rapid mergers”: When $t_{\text{GW}}(e_{\text{max}}) \lesssim t_{\text{LK}} j(e_{\text{max}})$, the binary is “pushed” into high eccentricity and exhibits a “one shot merger” without any e -oscillations.
- “Smooth mergers”: When $t_{\text{GW}}(e_{\text{max}}) \gtrsim t_{\text{LK}} j(e_{\text{max}})$, the binary goes through a phase of eccentricity oscillations while the orbit gradually decays. In this case, the LK-averaged orbital decay rate is $\sim j(e_{\text{max}}) t_{\text{GW}}^{-1}(e_{\text{max}})$. As a decreases, e_{max} decreases slightly while the minimum eccentricity increases, approaching e_{max} (see Fig. 1). This eccentricity oscillation “freeze” ($e_{\text{min}} \sim e_{\text{max}}$) is due to GR-induced apsidal precession (ϵ_{GR} increases as a decreases), and occurs when $\epsilon_{\text{GR}}(a) \gg j(e_{\text{max}})$. After the eccentricity is frozen, the binary circularizes and decays on the timescale $t_{\text{GW}}(e_{\text{max}})$.

III. SPIN DYNAMICS: EQUATIONS

We are interested in the spin orientations of the inner BHs at merger as a function of initial conditions. Since they evolve independently to leading post-Newtonian order, we focus on the dynamics of $\hat{\mathbf{S}}_1 = \hat{\mathbf{S}}$, the unit spin vector of m_1 . Since the spin magnitude does not enter into the dynamics, we write $\mathbf{S} \equiv \hat{\mathbf{S}}$ for brevity (i.e. \mathbf{S} is a unit vector). Neglecting spin-spin interactions, \mathbf{S} undergoes de Sitter precession about \mathbf{L} as

$$\frac{d\mathbf{S}}{dt} = \Omega_{\text{SL}} \hat{\mathbf{L}} \times \mathbf{S}, \quad (20)$$

with

$$\Omega_{\text{SL}} = \frac{3Gn(m_2 + \mu/3)}{2c^2 a j^2(e)}. \quad (21)$$

In the presence of a tertiary companion, the orbital axis $\hat{\mathbf{L}}$ of the inner binary precesses around $\hat{\mathbf{L}}_{\text{out}}$ with rate $d\delta\mathcal{Q}/dt$ and nutates with varying I [see Eqs. (5) and (6)]. To analyze the dynamics of the spin vector, we go to the co-rotating frame with $\hat{\mathbf{L}}$ about $\hat{\mathbf{L}}_{\text{out}}$, in which Eq. (20) becomes

$$\left(\frac{d\mathbf{S}}{dt} \right)_{\text{rot}} = \mathbf{\Omega}_e \times \mathbf{S}, \quad (22)$$

where we have defined an effective rotation vector

$$\mathbf{\Omega}_e \equiv \Omega_{\text{L}} \hat{\mathbf{L}}_{\text{out}} + \Omega_{\text{SL}} \hat{\mathbf{L}}, \quad (23)$$

with [see Eq. (5)]

$$\Omega_{\text{L}} \equiv -\frac{d\delta\mathcal{Q}}{dt}. \quad (24)$$

In this rotating frame, the plane spanned by $\hat{\mathbf{L}}_{\text{out}}$ and $\hat{\mathbf{L}}$ is constant in time, only the inclination angle I can vary.

A. Nondissipative Spin Dynamics

We first consider the limit where dissipation via GW radiation is completely neglected ($t_{\text{GW}}(e) \rightarrow \infty$). Then $\mathbf{\Omega}_e$ is exactly periodic with period P_{LK} [see Eq. (19)] We can rewrite Eq. (22) in Fourier components

$$\left(\frac{d\mathbf{S}}{dt} \right)_{\text{rot}} = \left[\bar{\mathbf{\Omega}}_e + \sum_{N=1}^{\infty} \mathbf{\Omega}_{eN} \cos(N\Omega_{\text{LK}} t) \right] \times \mathbf{S}. \quad (25)$$

Note that $\bar{\mathbf{\Omega}}_e$ is the zeroth Fourier component, where the bar denotes an average over a LK cycle. We have adopted the convention where $t = 0$ is the time of maximum eccentricity of the LK cycle, so that Eq. (25) does not have $\sin(N\Omega_{\text{LK}} t)$ terms.

This system superficially resembles that considered in Storch and Lai [44] (SL15), who studied the dynamics of the spin axis of a star when driven by a giant planet undergoing LK oscillations [see also 45, 46]. In their system, the spin-orbit coupling arises from Newtonian interaction between the planet (M_p) and the rotation-induced stellar quadrupole ($I_3 - I_1$), and the spin precession frequency is

$$\Omega_{\text{SL}}^{(\text{Newtonian})} = -\frac{3GM_p(I_3 - I_1) \cos \theta_{\text{sl}}}{2a^3 j^3(e) I_3 \Omega_s}, \quad (26)$$

where $I_3 \Omega_s$ is the spin angular momentum of the star. SL15 showed that under some conditions that depend on a dimensionless adiabaticity parameter (roughly the ratio between the magnitudes of $\Omega_{\text{SL}}^{(\text{Newtonian})}$ and Ω_{L} when factoring out the eccentricity and obliquity dependence), the stellar spin axis can vary chaotically. One strong indicator of chaos in their study is the presence of irregular, fine structure in a bifurcation diagram [Fig. 1 of Storch and Lai [44]] that shows the values of the spin-orbit misalignment angle θ_{sl} when varying system parameters in the “transadiabatic” regime, where the adiabaticity parameter crosses unity.

To generate an analogous bifurcation diagram for our problem, we consider a sample system with $m_{12} = 60M_{\odot}$, $m_3 = 3 \times 10^7 M_{\odot}$, $a = 0.1$ AU, $e_0 = 10^{-3}$, $I_0 = 70^\circ$, $a_{\text{out}} = 300$ AU, $e_{\text{out}} = 0$, and initial $\theta_{\text{sl}} = 0$ (note that these parameters are different from those in Fig. 1). We then evolve Eq. (20) together with the orbital evolution equations [Eqs. (3–7) without the GW terms] while sampling both θ_{sl} and θ_e at eccentricity maxima, where θ_e is the angle between $\bar{\mathbf{\Omega}}_e$ and \mathbf{S} , i.e.

$$\cos \theta_e = \frac{\bar{\mathbf{\Omega}}_e}{\Omega_e} \cdot \mathbf{S}. \quad (27)$$

We repeat this procedure with different mass ratios m_1/m_{12} of the inner binary, which only changes Ω_{SL} without changing the orbital evolution (note that the LK oscillation depends only on m_{12} and not on individual masses of the inner binary). Analogous to SL15, we consider systems with a range of the adiabaticity parameter \mathcal{A} [to be defined later in Eq. (31)] that crosses order unity. Note that the fiducial system of Fig. 1 does not serve this purpose because the initial Ω_{SL} is too small. Our result is depicted in Fig. 3.

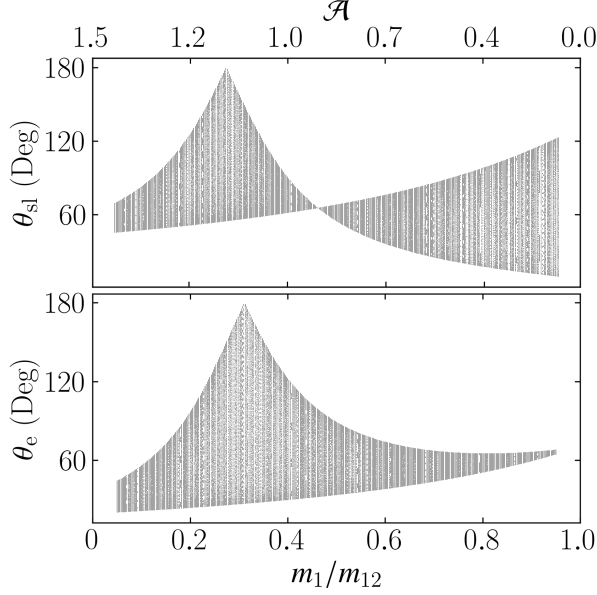


FIG. 3. Bifurcation diagram for the BH spin orientation during LK oscillations. The physical parameters are $m_{12} = 60M_{\odot}$, $m_3 = 3 \times 10^7 M_{\odot}$, $a = 0.1$ AU, $e_0 = 10^{-3}$, $I_0 = 70^\circ$, $a_{\text{out}} = 300$ AU, $e_{\text{out}} = 0$, and initial condition $\theta_{\text{sl},0} = 0$. For each mass ratio m_1/m_{12} , the orbit-spin system is solved over 500 LK cycles, and both θ_{sl} (the angle between \mathbf{S} and $\hat{\mathbf{L}}$) and θ_e [defined by Eq. (27)] are sampled at every eccentricity maximum and are plotted. The top axis shows the adiabaticity parameter \mathcal{A} as defined by Eq. (31). Note that for a given m_{12} , changing the mass ratio m_1/m_{12} only changes the spin evolution and not the orbital evolution.

While our bifurcation diagram has interesting structure, the features are all regular. This is in contrast to the star-planet system studied by SL15 (see their Fig. 1). A key difference is that in our system, Ω_{SL} does not depend on θ_{sl} , while for the planet-star system, $\Omega_{\text{SL}}^{(\text{Newtonian})}$ does, and this latter feature introduces nonlinearity to the dynamics.

A more formal understanding of the dynamical behavior of our spin-orbit system comes from Floquet theory[47, 48], as Eq. (22) is a linear system with periodic coefficients (the system studied in SL15 is nonlinear). By Floquet’s theorem, when a linear system with periodic coefficients is integrated over a period, the evolution can be described by the linear transformation

$$\mathbf{S}(t + P_{\text{LK}}) = \tilde{\mathbf{M}}\mathbf{S}(t), \quad (28)$$

where $\tilde{\mathbf{M}}$ is called the *monodromy matrix* and is independent of \mathbf{S} .

For our system, while $\tilde{\mathbf{M}}$ can be easily defined, it cannot be evaluated in closed form. Instead, we can reason directly about the general properties of $\tilde{\mathbf{M}}$: it must be a proper orthogonal matrix, or a rotation matrix, as it represents the effect of many infinitesimal rotations, each about the instantaneous $\bar{\Omega}_e$ [49]. Therefore, over each period P_{LK} , the dynamics of \mathbf{S} are equivalent to a rotation about a fixed axis, prohibiting chaotic behavior.

Another traditional indicator of chaos is a positive Lyapunov exponent, obtained when the separation between nearby trajectories diverges *exponentially* in time. In Floquet theory, the Lyapunov exponent is the logarithm of the largest eigenvalue of the monodromy matrix. Since $\tilde{\mathbf{M}}$ is a rotation matrix in our problem, the Lyapunov exponent must be 0, indicating no chaos. We have verified this numerically.

B. Spin Dynamics With GW Dissipation

When t_{GW} is finite, the coefficients Ω_{eN} , including $\bar{\Omega}_e$ [see Eq. (25)], are no longer constant, but change over time. For “smooth” mergers (satisfying $t_{\text{GW}}(e_{\text{max}}) \gg t_{\text{LK}}j(e_{\text{max}})$; see Section II), the binary goes through a sequence of LK cycles, and the coefficients vary on the LK-averaged orbital decay time $t_{\text{GW}}(e_{\text{max}})/j(e_{\text{max}})$. After the LK oscillation freezes, we have $\Omega_e \approx \bar{\Omega}_e$ (and $\Omega_{eN} \approx 0$ for $N \geq 1$), which evolves on timescale $t_{\text{GW}}(e)$ as the orbit decays and circularizes.

Once a is sufficiently small that $\Omega_{\text{SL}} \gg \Omega_L$, it can be seen from Eqs. (22–23) that $\theta_e = \theta_{\text{sl}}$ is constant, i.e. the spin-orbit misalignment angle is frozen (see bottom right panel of Fig. 1). This is the “final” spin-orbit misalignment, although the binary may still be far from the final merger. Note that at such separations, $\epsilon_{\text{GR}} \gg 1$ as well since $\Omega_{\text{SL}} \sim \Omega_{\text{GR}}$, and so LK eccentricity excitation is suppressed. For the fiducial examples depicted in Figs. 1–2, we stop the simulation at $a = 0.5$ AU, as θ_{sl} has converged to its final value.

C. Spin Dynamics Equation in Component Form

For later analysis, it is useful to write Eq. (25) in component form. To do so, we define the inclination angle \bar{I}_e as the angle between $\bar{\Omega}_e$ and \mathbf{L}_{out} as shown in Fig. 4. To express \bar{I}_e algebraically, we define the LK-averaged quantities

$$\overline{\Omega_{\text{SL}} \sin \bar{I}} \equiv \bar{\Omega}_{\text{SL}} \sin \bar{I}, \quad \overline{\Omega_{\text{SL}} \cos \bar{I}} \equiv \bar{\Omega}_{\text{SL}} \cos \bar{I}. \quad (29)$$

It then follows from Eq. (23) that

$$\tan \bar{I}_e = \frac{\mathcal{A} \sin \bar{I}}{1 + \mathcal{A} \cos \bar{I}}, \quad (30)$$

where \mathcal{A} is the adiabaticity parameter, given by

$$\mathcal{A} \equiv \frac{\bar{\Omega}_{\text{SL}}}{\Omega_L}. \quad (31)$$

Note that in Eq. (30), \bar{I}_e is defined in the domain $[0^\circ, 180^\circ]$, i.e. $\bar{I}_e \in (0, 90)$ when $\tan \bar{I}_e > 0$ and $\bar{I}_e \in (90, 180)$ when $\tan \bar{I}_e < 0$.

We now choose a non-inertial coordinate system where $\hat{\mathbf{z}} \propto \bar{\Omega}_e$ and $\hat{\mathbf{x}}$ lies in the plane of \mathbf{L}_{out} and \mathbf{L} (see Fig. 4). In this reference frame, the spin orientation is specified by the polar angle θ_e as defined above in Eq. (27), and the spin evolution

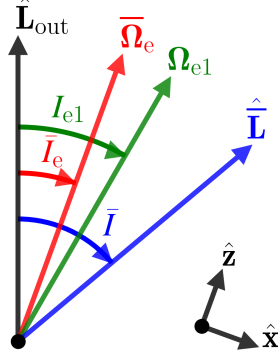


FIG. 4. Definition of angles in the problem, shown in plane of the two angular momenta \mathbf{L}_{out} and \mathbf{L} . Here, $\bar{\mathbf{L}}$ is the suitably averaged \mathbf{L} with inclination \bar{I} defined by Eq. (29), $\bar{\Omega}_e$ is the LK-averaged Ω_e , and Ω_{e1} is the first harmonic component (see Eqs. (23) and (25)). Note that for $I_0 > 90^\circ$ (and $\bar{I} > 90^\circ$), we choose $\bar{I}_e \in (90^\circ, 180^\circ)$ so that $\bar{\Omega}_e > 0$ (since $\Omega_L < 0$). The bottom right shows our choice of coordinate axes with $\hat{\mathbf{z}} \propto \bar{\Omega}_e$.

equation becomes

$$\left(\frac{d\mathbf{S}}{dt}\right)_{\text{xyz}} = \left[\bar{\Omega}_e \hat{\mathbf{z}} + \sum_{N=1}^{\infty} \Omega_{eN} \cos(N\Omega_{LK}t) \right] \times \mathbf{S} - \dot{I}_e \hat{\mathbf{y}} \times \mathbf{S}. \quad (32)$$

One further simplification lets us cast this vector equation of motion into a scalar form. Break \mathbf{S} into components $\mathbf{S} = S_x \hat{\mathbf{x}} + S_y \hat{\mathbf{y}} + \cos \theta_e \hat{\mathbf{z}}$ and define complex variable

$$S_{\perp} \equiv S_x + iS_y. \quad (33)$$

Then, we can rewrite Eq. (32) as

$$\frac{dS_{\perp}}{dt} = i\bar{\Omega}_e S_{\perp} - \dot{I}_e \cos \theta_e + \sum_{N=1}^{\infty} \left[\cos(\Delta I_{eN}) S_{\perp} - i \cos \theta_e \sin(\Delta I_{eN}) \right] \Omega_{eN} \cos(N\Omega_{LK}t), \quad (34)$$

where $\dot{I}_e = d\bar{I}_e/dt$ and Ω_{eN} is the magnitude of the vector Ω_{eN} [see Eq. (25)] and $\Delta I_{eN} = I_{eN} - \bar{I}_e$, with I_{eN} the angle between Ω_{eN} and \mathbf{L}_{out} (see Fig. 4). Since $\cos \theta_e = \pm \sqrt{1 - |S_{\perp}|^2}$, Eq. (34) is generally nonlinear in S_{\perp} , but becomes approximately linear when $|\theta_e| \ll 1$.

IV. ANALYSIS: APPROXIMATE ADIABATIC INVARIANT

In general, Eqs. (25) and (34) are difficult to study analytically. In this section, we neglect the harmonic terms and focus on how the varying $\bar{\Omega}_e$ affects the evolution of the BH spin axis. The effect of the harmonic terms is studied in Section V.

A. The Adiabatic Invariant

When neglecting the $N \geq 1$ harmonic terms, Eq. (25) reduces to

$$\left(\frac{d\bar{\mathbf{S}}}{dt}\right)_{\text{rot}} = \bar{\Omega}_e \times \bar{\mathbf{S}}. \quad (35)$$

It is not obvious to what extent the analysis of Eq. (35) is applicable to Eq. (25). From our numerical calculations, we find that the LK-average of \mathbf{S} often evolves following Eq. (35), motivating our notation $\bar{\mathbf{S}}$. Over timescales shorter than the LK period P_{LK} , Eq. (35) loses accuracy as the evolution of \mathbf{S} itself is dominated by the $N \geq 1$ harmonics we have neglected. An intuitive interpretation of this result is that the $N \geq 1$ harmonics vanish when integrating Eq. (25) over a LK cycle.

Eq. (35) has one desirable property: $\bar{\theta}_e$, defined by

$$\cos \bar{\theta}_e \equiv \frac{\bar{\Omega}_e}{\bar{\Omega}_e} \cdot \bar{\mathbf{S}}, \quad (36)$$

is an adiabatic invariant. This follows from the fact that $\bar{\mathbf{S}}_z$, the projection of $\bar{\mathbf{S}}$ on the $\bar{\Omega}_e$ axis, and φ , the precessional angle of $\bar{\mathbf{S}}$ around $\bar{\Omega}_e$, form a pair of action-angle variables. The adiabaticity condition requires that the precession axis $\hat{\mathbf{z}} = \bar{\Omega}_e/\bar{\Omega}_e$ evolve slowly compared to the precession frequency at all times, i.e.

$$\left|\frac{d\bar{I}_e}{dt}\right| \ll \bar{\Omega}_e. \quad (37)$$

For our fiducial example depicted in Fig. 1, the values of \dot{I}_e and $\bar{\Omega}_e$ are shown in the top panel of Fig. 5, and the evolution of $\bar{\theta}_e$ in the bottom panel. The net change in $\bar{\theta}_e$ in this simulation is 0.01° , small as expected since $|\dot{I}_e| \ll \bar{\Omega}_e$ at all times.

B. Deviation from Adiabaticity

The extent to which $\bar{\theta}_e$ is conserved depends on how well Eq. (37) is satisfied. In this subsection, we derive a bound on the total non-conservation of $\bar{\theta}_e$, then in the next subsection we show how this bound can be estimated from the initial conditions.

When neglecting harmonic terms, the scalar evolution equation Eq. (34) becomes

$$\frac{dS_{\perp}}{dt} = i\bar{\Omega}_e S_{\perp} - \dot{I}_e \cos \bar{\theta}_e. \quad (38)$$

This can be solved in closed form. Defining

$$\Phi(t) \equiv \int^t \bar{\Omega}_e dt, \quad (39)$$

we obtain the solution at time t :

$$e^{-i\Phi} S_{\perp} \Big|_0^t = - \int_0^t e^{-i\Phi(\tau)} \dot{I}_e \cos \bar{\theta}_e d\tau. \quad (40)$$

Recalling $|S_\perp| = \sin \bar{\theta}_e$ and analyzing Eq. (40), we see that $\bar{\theta}_e$ oscillates about its initial value with semi-amplitude

$$|\Delta \bar{\theta}_e| \sim \left| \frac{\dot{\bar{I}}_e}{\bar{\Omega}_e} \right|. \quad (41)$$

In the adiabatic limit [Eq. (37)], $\bar{\theta}_e$ is indeed conserved, as the right-hand side of Eq. (41) goes to zero. The bottom panel of Fig. 5 shows $\Delta \bar{\theta}_e$ for the fiducial example. Note that $\bar{\theta}_e$ is indeed mostly constant where Eq. (41) predicts small oscillations.

If we denote $|\Delta \bar{\theta}_e|_f$ to be the net change in $\bar{\theta}_e$ over $t \in [0, t_f]$, we can give a loose bound

$$|\Delta \bar{\theta}_e|_f \lesssim \left| \frac{\dot{\bar{I}}_e}{\bar{\Omega}_e} \right|_{\max}. \quad (42)$$

Inspection of Fig. 5 indicates that the spin dynamics are mostly uninteresting except near the peak of $|\dot{\bar{I}}_e|$, which occurs where $\bar{\Omega}_{SL} \approx |\Omega_L|$. We present a zoomed-in view of dynamical quantities near the peak of $|\dot{\bar{I}}_e|$ in Fig. 6. In particular, in the bottom-rightmost panel, we see that the fluctuations in $\bar{\theta}_e$ are dominated by a second contribution, the subject of the discussion in Section V.

For comparison, we show in Fig. 7 a more rapid binary merger starting with $I_0 = 90.2^\circ$, for which $|\Delta \theta_e|_f \approx 2^\circ$. If we again examine the bottom-rightmost panel, we see that the net $|\Delta \bar{\theta}_e|_f$ obeys Eq. (42).

C. Estimate of Deviation from Adiabaticity from Initial Conditions

To estimate Eq. (42) as a function of initial conditions, we first differentiate Eq. (30),

$$\dot{\bar{I}}_e = \left(\frac{\dot{\mathcal{A}}}{\mathcal{A}} \right) \frac{\mathcal{A} \sin \bar{I}}{1 + 2\mathcal{A} \cos \bar{I} + \mathcal{A}^2}. \quad (43)$$

It also follows from Eq. (23) that

$$\bar{\Omega}_e = \left| \bar{\Omega}_L \right| \left(1 + 2\mathcal{A} \cos \bar{I} + \mathcal{A}^2 \right)^{1/2}, \quad (44)$$

from which we obtain

$$\left| \frac{\dot{\bar{I}}_e}{\bar{\Omega}_e} \right| = \left(\frac{\dot{\mathcal{A}}}{\mathcal{A}} \right) \frac{1}{\left| \bar{\Omega}_L \right|} \frac{\mathcal{A} \sin \bar{I}}{(1 + 2\mathcal{A} \cos \bar{I} + \mathcal{A}^2)^{3/2}}. \quad (45)$$

Moreover, if we assume the eccentricity is frozen around $e \approx 1$ and use $\cos^2 \omega \approx 1/2$ in $|\Omega_L| = |d\phi/dt|$, we obtain the estimate

$$\begin{aligned} \mathcal{A} &= \frac{\bar{\Omega}_{SL}}{\bar{\Omega}_L} \approx \frac{3Gn(m_2 + \mu/3)}{2c^2 a j^2(e)} \left[\frac{15 \cos \bar{I}}{8 t_{LK} j(e)} \right]^{-1} \\ &\approx \frac{4}{5} \frac{G(m_2 + \mu/3) m_{12} \tilde{a}_{\text{out}}^3}{c^2 m_3 a^4 j(e) \cos \bar{I}}, \end{aligned} \quad (46)$$

$$\frac{\dot{\mathcal{A}}}{\mathcal{A}} = -4 \left(\frac{\dot{a}}{a} \right)_{\text{GW}} + \frac{e}{j^2(e)} \left(\frac{de}{dt} \right)_{\text{GW}}. \quad (47)$$

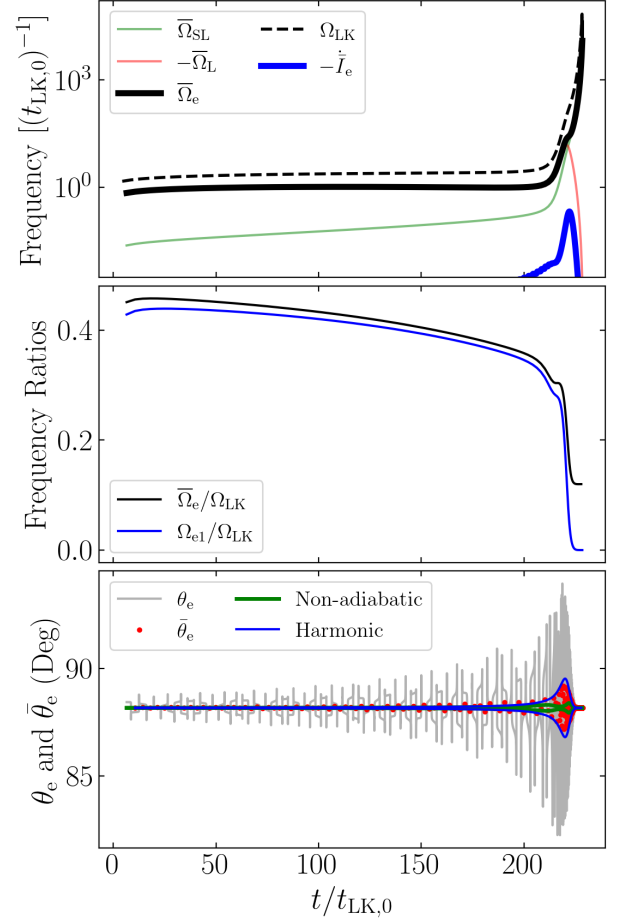


FIG. 5. The same simulation as depicted in Fig. 1 but showing several calculated quantities relevant to the theory of the spin evolution. Top: the four characteristic frequencies of the system and $d\bar{I}_e/dt$. Middle: the frequency ratios between the zeroth and first Fourier components of Ω_e to the LK frequency Ω_{LK} . Bottom: Time evolution of θ_e [grey line; Eq. (27)], $\bar{\theta}_e$ [red dots; Eq. (36)], as well as estimates of the deviations from perfect conservation of $\bar{\theta}_e$ due to nonadiabaticity [green, Eq. (41)] and due to the resonance $\bar{\Omega}_e \approx \Omega_{LK}$ [blue, Eq. (81)].

With these, we see that Eq. (45) is largest around $\mathcal{A} \approx 1$, and so we find that the maximum $|\dot{\bar{I}}_e|/\bar{\Omega}_e$ is given by

$$\left| \frac{\dot{\bar{I}}_e}{\bar{\Omega}_e} \right|_{\max} \approx \left| \frac{\dot{\mathcal{A}}}{\mathcal{A}} \right| \frac{1}{\left| \bar{\Omega}_L \right|} \frac{\sin \bar{I}}{(2 + 2 \cos \bar{I})^{3/2}}. \quad (48)$$

To evaluate this, we make two assumptions: (i) \bar{I} is approximately constant (see the third panels of Figs. 6 and 7), and (ii) $j(e)$ evaluated at $\mathcal{A} \approx 1$ can be approximated as a constant multiple of the initial $j(e_{\max})$, i.e.

$$j_\star \equiv j(e_\star) = f \sqrt{\frac{5}{3}} \cos^2 I_0, \quad (49)$$

where the star subscript denotes evaluation at $\mathcal{A} \approx 1$ and $f > 1$ is a constant. Eq. (49) assumes that I_0 far enough from 90°

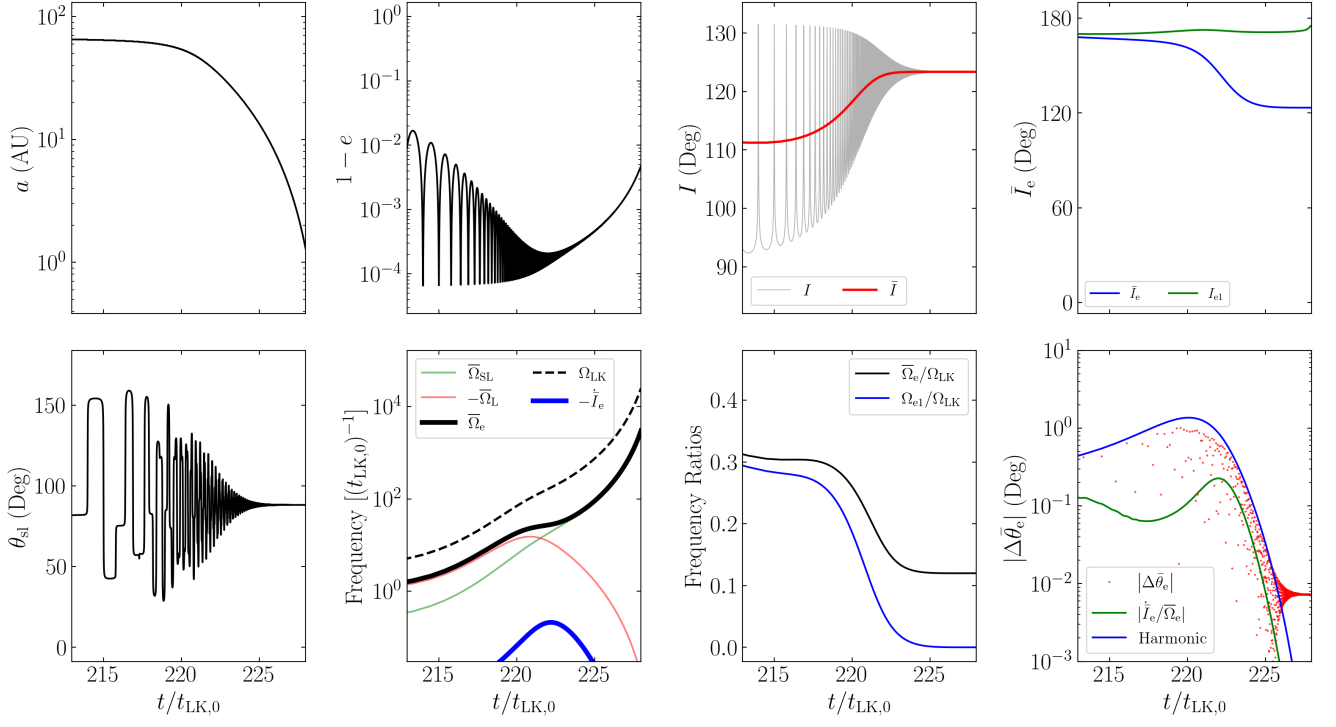


FIG. 6. The same simulation as Fig. 1 but zoomed in on the region around $\mathcal{A} \equiv \bar{\Omega}_{\text{SL}}/\bar{\Omega}_{\text{L}} \approx 1$ and showing a wide range of relevant quantities. The first three panels in the upper row depict a , e , I and \bar{I} as in Fig. 1, while the fourth shows \bar{I}_e [Eq. (30)] and I_{e1} . The bottom four panels depict θ_{sl} , the four characteristic frequencies of the system and $d\bar{I}_e/dt$ [Eqs. 23 and (24)] (as in the top panel of Fig. 5), the relevant frequency ratios (as in the middle panel of Fig. 5), and the deviation of $\bar{\theta}_e$ from its initial value compared to the predictions of Eqs. (41) and (81).

that the GR effect is unimportant in determining e_{max} . The value of f turns out to be relatively insensitive to I_0 .

Using Eq. (47) and approximating $e_{\star} \approx 1$ in Eqs. (11) and (12) give

$$\left[\frac{\mathcal{A}}{\mathcal{A}} \right]_{\star} \approx \frac{G^3 \mu m_{12}^2 595}{c^5 a_{\star}^4 j_{\star}^7 3}. \quad (50)$$

To determine a_{\star} , we require Eq. (46) to give $\mathcal{A} = 1$ for a_{\star} and j_{\star} . Taking this and Eq. (50), we rewrite Eq. (45) as

$$\left| \frac{\dot{\bar{I}}_e}{\bar{\Omega}_e} \right|_{\text{max}} \approx \frac{595 \sin \bar{I} |\cos \bar{I}|^{3/8}}{36 (\cos \bar{I} + 1)^{3/2}} \left[\frac{8000 G^9 m_{12}^9 m_3^3 \mu^8}{\tilde{a}_{\text{out}}^9 j_{\star}^{37} c^{18} (m_2 + \mu/3)^{11}} \right]^{1/8}. \quad (51)$$

We can also calculate $|\dot{\bar{I}}_e|/\bar{\Omega}_e$ from numerical simulations. Taking characteristic $\bar{I} \approx 120^\circ$ (Figs. 6 and 7 show that this holds across a range of I_0), we fit the last remaining free parameter f [Eq. (49)] to the data from numerical simulations. This yields $f \approx 2.72$, leading to

$$\left| \frac{\dot{\bar{I}}_e}{\bar{\Omega}_e} \right|_{\text{max}} \approx 0.98^\circ \left(\frac{\cos I_0}{\cos(90.3^\circ)} \right)^{-37/8} \left(\frac{\tilde{a}_{\text{out}}}{2.2 \text{ pc}} \right)^{-9/8} \times \left(\frac{m_3}{3 \times 10^7 M_\odot} \right)^{3/8} \left(\frac{m_{12}^9 \mu^8 / (m_2 + \mu/3)^{11}}{(28.64 M_\odot)^6} \right)^{1/8}. \quad (52)$$

Fig. 8 shows that when the merger time T_m is much larger than the initial LK timescale, Eq. (52) provides an accurate estimate for $|\dot{\bar{I}}_e/\bar{\Omega}_e|_{\text{max}}$ when compared with numerical results.

In the above, we have assumed that the system evolves through $\mathcal{A} \approx 1$ when the eccentricity is mostly frozen (see Fig. 1 for an indication of how accurate this is for the parameter space explored in Fig. 8). It is also possible that $\mathcal{A} \approx 1$ occurs when the eccentricity is still undergoing substantial oscillations. In fact, Eq. (52) remains accurate in this case when replacing e with e_{max} , due to the following analysis. Recall that when $e_{\text{min}} \ll e_{\text{max}}$, the binary spends a fraction $\sim j(e_{\text{max}})$ of the LK cycle near $e \approx e_{\text{max}}$. This fraction of the LK cycle dominates both GW dissipation and $\bar{\Omega}_e$ precession. Thus, both $\dot{\bar{I}}_e$ and $\bar{\Omega}_e$ in the **eccentricity-oscillating** regime can be evaluated by setting $e \approx e_{\text{max}}$ and multiplying by a prefactor of $j(e_{\text{max}})$. This factor cancels when computing the quotient $|\dot{\bar{I}}_e|/\bar{\Omega}_e$.

The accuracy of Eq. (52) in bounding $|\Delta \bar{\theta}_e|_f$ is shown in Fig. 9, where we carry out simulations for a range of I_0 , and for each I_0 we consider 100 different, isotropically distributed initial orientations for \mathbf{S} (thus sampling a wide range of initial $\bar{\theta}_e$). Note that conservation of $\bar{\theta}_e$ is generally much better than Eq. (52) predicts. This is because cancellation of phases in Eq. (40) is generally more efficient than Eq. (52) assumes (recall that Eq. (41) only provides an estimate for the amplitude of “local” oscillations of $\bar{\theta}_e$). Nevertheless, it is

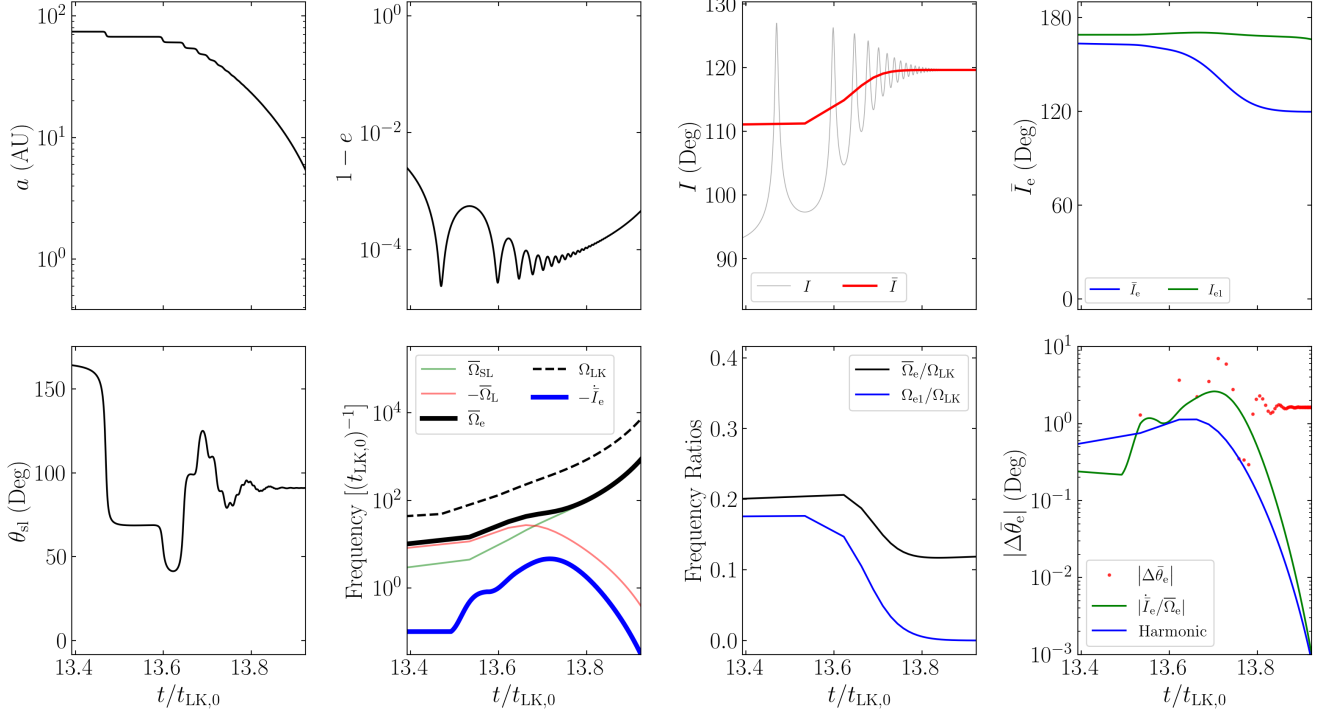


FIG. 7. Same as Fig. 6 except for $I_0 = 90.2^\circ$ (and all other parameters are the same as in Fig. 1), corresponding to a faster coalescence. The total change in $\bar{\theta}_e$ for this simulation is $\approx 2^\circ$.

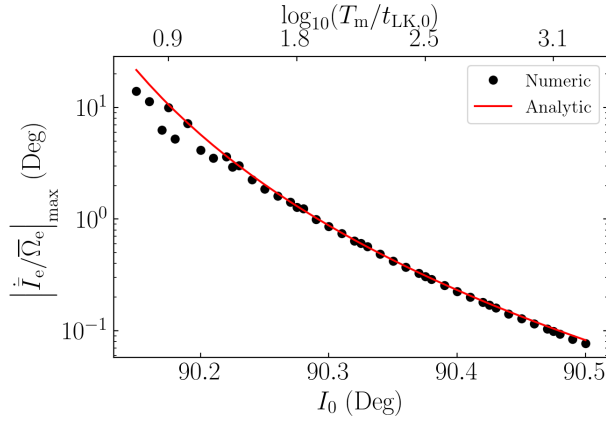


FIG. 8. Comparison of $|\dot{\bar{\theta}}_e/\bar{\Omega}_e|_{\max}$ obtained from simulations and from the analytical expression Eq. (52), where we take $f = 2.72$ in Eq. (49). The merger time T_m is shown along the top axis of the plot in units of the initial LK timescale $t_{LK,0}$. The agreement between the analytical and numerical results is excellent for $T_m \gg t_{LK,0}$.

clear that Eq. (52) provides a robust upper bound of $|\Delta\bar{\theta}_e|_f$, and serves as a good indicator for the breakdown of adiabatic invariance.

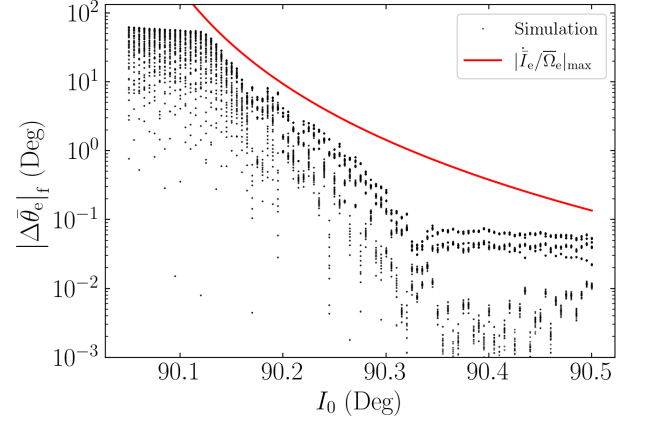


FIG. 9. Net change in $\bar{\theta}_e$ over the binary inspiral as a function of initial inclination I_0 . For each I_0 , 100 simulations are run for \mathbf{S} on a uniform, isotropic grid. Plotted for comparison is the bound $|\Delta\bar{\theta}_e|_f \lesssim |\dot{\bar{I}}_e/\bar{\Omega}_e|_{\max}$, using the analytical expression given by Eq. (52). It is clear that the expression provides a robust upper bound for the non-conservation of $\bar{\theta}_e$ due to nonadiabatic effects. Note that at the right of the plot, the numerical $|\Delta\bar{\theta}_e|_f$ saturates; this is because we compute the initial $\bar{\Omega}_e$ (in order to evaluate the initial $\bar{\theta}_e$) without GW dissipation, and such a procedure inevitably introduces fuzziness in $\bar{\theta}_e$.

D. Origin of the $\theta_{\text{sl},f} = 90^\circ$ Attractor

Using the approximate adiabatic invariant, we can now understand the origin of the $\theta_{\text{sl},f} = 90^\circ$ attractor as shown in Fig. 2.

Recall from Eq. (23)

$$\begin{aligned}\bar{\Omega}_e &= \bar{\Omega}_L \hat{\mathbf{L}}_{\text{out}} + \overline{\Omega_{\text{SL}}} \hat{\mathbf{L}}, \\ &= (\bar{\Omega}_L + \bar{\Omega}_{\text{SL}} \cos \bar{I}) \hat{\mathbf{Z}} + \bar{\Omega}_{\text{SL}} \sin \bar{I} \hat{\mathbf{X}},\end{aligned}\quad (53)$$

where $\hat{\mathbf{Z}} = \hat{\mathbf{L}}_{\text{out}}$ and $\hat{\mathbf{X}}$ is perpendicular to $\hat{\mathbf{Z}}$ in the $\hat{\mathbf{L}}_{\text{out}}-\hat{\mathbf{L}}$ plane. Note that

$$\bar{\Omega}_L \propto \frac{\cos \bar{I}}{t_{\text{LK}}} \propto a^{3/2} \cos \bar{I}, \quad (54)$$

$$\bar{\Omega}_{\text{SL}} \propto \frac{1}{a^{5/2}}. \quad (55)$$

Adiabatic invariance implies that $\bar{\theta}_e$, the angle between \mathbf{S} and $\bar{\Omega}_e$ is conserved between $t = 0$ and $t = t_f$, i.e.

$$\bar{\theta}_{e,f} \simeq \bar{\theta}_{e,0}. \quad (56)$$

At $t = t_f$, $\bar{\Omega}_{\text{SL}} \gg |\bar{\Omega}_L|$ and the spin-orbit misalignment angle θ_{sl} is “frozen”, implying $\bar{\Omega}_e$ is parallel to \mathbf{L} , and so $\bar{\theta}_{e,f} = \theta_{\text{sl},f}$. Eq. (56) then gives

$$\theta_{\text{sl},f} \simeq \bar{\theta}_{e,0}, \quad (57)$$

i.e. the final θ_{sl} is determined by the initial angle between \mathbf{S} and $\bar{\Omega}_e$.

Now, first consider the case where the initial spin \mathbf{S}_0 is aligned with the initial \mathbf{L}_0 . This initial spin is inclined with respect to $\bar{\Omega}_e$ by $\bar{\theta}_{e,0} = |I_0 - \bar{I}_{e,0}|$, where I_0 is the initial inclination angle between \mathbf{L} and \mathbf{L}_{out} and $\bar{I}_{e,0}$ is the initial value of \bar{I}_e . Thus, adiabatic invariance implies

$$\theta_{\text{sl},f} \simeq |I_0 - \bar{I}_{e,0}|. \quad (58)$$

In the special case where the binary initially satisfies $\bar{\Omega}_{\text{SL}} \ll |\bar{\Omega}_L|$ or $|\mathcal{A}_0| \ll 1$, we find that $\bar{\Omega}_e$ is nearly parallel to \mathbf{L}_{out} (for $I_0 < 90^\circ$) or antiparallel to \mathbf{L}_{out} (for $I_0 > 90^\circ$). Thus,

$$\theta_{\text{sl},f} = \begin{cases} I_0 & I_0 < 90^\circ, \\ 180^\circ - I_0 & I_0 > 90^\circ. \end{cases} \quad (59)$$

Since LK-induced mergers necessarily require I_0 close to 90° , we find that $\theta_{\text{sl},f}$ is “attracted” to 90° .

Eq. (57) can be applied to more general initial spin orientations. For initial $|\mathcal{A}_0| \ll 1$ (as required for LK-induced mergers), $\bar{\Omega}_{e,0}$ is parallel to $\pm \mathbf{L}_{\text{out}}$. Suppose the initial inclination between \mathbf{S} and \mathbf{L}_{out} is $\theta_{s,\text{out},0}$, then $\bar{\theta}_{e,0} = \theta_{s,\text{out},0}$ or $180^\circ - \theta_{s,\text{out},0}$ (depending on whether $I_0 < 90^\circ$ or $I_0 > 90^\circ$). Thus,

$$\theta_{\text{sl},f} \simeq \begin{cases} \theta_{s,\text{out},0} & I_0 < 90^\circ, \\ 180^\circ - \theta_{s,\text{out},0} & I_0 > 90^\circ, \end{cases} \quad (60)$$

[see also 50].

So far, we have analyzed the $\theta_{\text{sl},f}$ distribution for smooth mergers. Next, we can consider rapid mergers, for which $\bar{\theta}_e$ conservation is imperfect. We expect

$$|\theta_{\text{sl},f} - \bar{\theta}_{e,0}| \lesssim |\Delta \bar{\theta}_e|_f. \quad (61)$$

where $|\Delta \bar{\theta}_e|_f$ is given by Eq. (52). This is shown as the black dotted line in Fig. 2, and we see it predicts the maximum deviation of $\theta_{\text{sl},f}$ from $\sim 90^\circ$ except very near $I_0 = 90^\circ$. This is expected, as Eq. (52) is not very accurate very near $I_0 = 90^\circ$, where it diverges (see Fig. 9).

When $I_0 = 90^\circ$ exactly, Fig. 2 shows that $\theta_{\text{sl},f} = 0^\circ$. This can be understood: $I_0 = 90^\circ$ gives $dI/dt = 0$ by Eq. (6), so $I = 90^\circ$ for all time. This then yields $d\bar{\Omega}/dt = 0$ [Eq. (5)], implying that \mathbf{L} is constant. Thus, \mathbf{L} is fixed as \mathbf{S} precesses around it, and θ_{sl} can never change. In Fig. 2, we take $\theta_{\text{sl},0} = 0$, so $\theta_{\text{sl},f} = 0$.

Finally, Fig. 2 shows that the actual $\theta_{\text{sl},f}$ are oscillatory within the envelope bounded by Eq. (61) above. This can also be understood: Eq. (42) only bounds the maximum of the absolute value of the change in $\bar{\theta}_e$, while the actual change depends on the initial and final complex phases of S_\perp in Eq. (40), denoted $\Phi(0)$ and $\Phi(t_f)$. When $\theta_{\text{sl},0} = 0$, we have $\Phi(0) = 0$, as \mathbf{S} starts in the $\hat{\mathbf{x}}-\hat{\mathbf{z}}$ plane. Then, as I_0 is smoothly varied, the final phase $\Phi(t_f)$ must also vary smoothly [since $\bar{\Omega}_e$ in Eq. (39) is a continuous function, $\Phi(t)$ must be as well], so the total phase difference between the initial and final values of S_\perp varies smoothly. This means the total change in $\bar{\theta}_e$ will fluctuate smoothly between $\pm |\Delta \bar{\theta}_e|_f$ as I_0 is changed, giving rise to the sinusoidal shape seen in Fig. 2.

V. ANALYSIS: EFFECT OF RESONANCES

In the previous section, we have shown that the $\theta_{\text{sl},f}$ distribution in Fig. 2 and the “ 90° attractor” can be understood when neglecting the $N \geq 1$ Fourier harmonics in Eq. (25). In this section, we study the effects of these neglected terms and show that they have a negligible effect in LK-induced mergers. Separately, we will also consider the LK-enhanced regime and show that these Fourier harmonics play a dominant role in shaping the $\theta_{\text{sl},f}$ distribution.

For simplicity, we ignore the effects of GW dissipation in this section and assume the system is exactly periodic (so $\dot{I}_e = 0$). The scalar spin evolution equation Eq. (34) is then

$$\begin{aligned}\frac{dS_\perp}{dt} &= i\bar{\Omega}_e S_\perp + \sum_{N=1}^{\infty} \left[\cos(\Delta I_{eN}) S_\perp \right. \\ &\quad \left. - i \cos \theta_e \sin(\Delta I_{eN}) \right] \Omega_{eN} \cos(N\Omega_{\text{LK}} t). \end{aligned} \quad (62)$$

A. Intuitive Analysis

We first restrict our attention to the effect of just the N -th Fourier harmonic, and Eq. (62) further simplifies to

$$\frac{dS_{\perp}}{dt} = \left[i\bar{\Omega}_e + \Omega_{eN} \cos(\Delta I_{eN}) \cos(N\Omega_{LK}t) \right] S_{\perp} - i\Omega_{eN} \cos \bar{\theta}_e \sin(\Delta I_{eN}) \cos(N\Omega_{LK}t). \quad (63)$$

There are two time-dependent perturbations, a modulation of the oscillation frequency (**the term proportional to S_{\perp} on the right-hand side**) and a driving term. We can begin to understand the dynamics of S_{\perp} by considering the effect of each of these two terms **separately**.

First, we consider the effect of frequency modulation alone. The equation of motion is

$$\frac{dS_{\perp}}{dt} \approx \left[i\bar{\Omega}_e + \Omega_{eN} \cos(\Delta I_{eN}) \cos(N\Omega_{LK}t) \right] S_{\perp}. \quad (64)$$

The exact solution is

$$S_{\perp}(t) = S_{\perp}(0) \exp \left[i\bar{\Omega}_e t + \frac{\Omega_{eN} \cos(\Delta I_{eN})}{N\Omega_{LK}} \sin(N\Omega_{LK}t) \right]. \quad (65)$$

There is no combination of parameters for which the magnitude of S_{\perp} diverges, so the modulation of the oscillation frequency does not cause any resonant behavior.

When considering only the time-dependent driving term instead, the equation of motion is

$$\frac{dS_{\perp}}{dt} \approx i\bar{\Omega}_e S_{\perp} - i\Omega_{eN} \cos \theta_e \sin(\Delta I_{eN}) \cos(N\Omega_{LK}t). \quad (66)$$

We can approximate $\cos(N\Omega_{LK}t) \approx e^{iN\Omega_{LK}t}/2$, as the $e^{-iN\Omega_{LK}t}$ component is always farther from resonance (as $\Omega_{LK}, \bar{\Omega}_e > 0$). Then the equation of motion has the solution

$$e^{-i\bar{\Omega}_e t} S_{\perp} \Big|_0^t = - \int_0^t \frac{i\Omega_{eN} \sin(\Delta I_{eN})}{2} e^{-i\bar{\Omega}_e t + iN\Omega_{LK}t} \cos \theta_e dt. \quad (67)$$

Since $|S_{\perp}| = \sin \theta_e$, the instantaneous oscillation amplitude $|\Delta \theta_e|$ can be bound by

$$|\Delta \theta_e| \sim \frac{1}{2} \left| \frac{\Omega_{eN} \sin(\Delta I_{eN})}{\bar{\Omega}_e - N\Omega_{LK}} \right|. \quad (68)$$

Thus, we see that large oscillation amplitudes in $\bar{\theta}_e$ occur when $\bar{\Omega}_e \approx N\Omega_{LK}$, the frequency of the N -th Fourier harmonic.

B. General Solution

1. Single Fourier Harmonic

Above, we began the analysis of Eq. (63) by considering the two time-dependent perturbations separately. However, this is

not necessary. Eq. (63) can be solved exactly:

$$\begin{aligned} e^{-i\Phi} S_{\perp} \Big|_0^t &= -i\Omega_{eN} \cos \bar{\theta}_e \sin \Delta I_{eN} \int_0^t \cos(N\Omega\tau) e^{-i\Phi(\tau)} d\tau, \\ &= iA \left[e^{-i\Phi} \Big|_0^t + i\bar{\Omega}_e \int_0^t e^{-i\Phi(\tau)} d\tau \right]. \end{aligned} \quad (69)$$

where $A = -\tan \Delta I_{eN} \cos \bar{\theta}_e$, and

$$\begin{aligned} i\Phi(t) &\equiv \int_0^t i\bar{\Omega}_e + \Omega_{eN} \cos(N\Omega_{LK}\tau) \cos(\Delta I_{eN}) d\tau, \\ &\equiv i\bar{\Omega}_e t + \eta \sin(N\Omega_{LK}t), \end{aligned} \quad (70)$$

where $\eta \equiv (\Omega_{eN} \cos \Delta I_{eN}) / (N\Omega_{LK})$. Eq. (69) shows that $|S_{\perp}|$ is bounded for all t unless the integral $I(x)$, given by

$$I(x) = \int_0^x e^{-i\xi - \eta \sin(\beta\xi)} d\xi, \quad (71)$$

grows without bound as $x \rightarrow \infty$, where $x = \bar{\Omega}_e t$ and $\beta = N\Omega_{LK}/\bar{\Omega}_e$.

To see where $I(x)$ grows without bound, we rewrite

$$I(x) = \sum_{k=0}^{\infty} \int_0^x (\cos \xi + i \sin \xi) \frac{(-\eta \sin(\beta\xi))^k}{k!} d\xi. \quad (72)$$

These $\sin^k(\beta\xi)$ terms can be expanded using the general trigonometric power-reduction identities [51]:

$$\sin^{2n} y = \frac{1}{2^{2n}} \binom{2n}{n} + \frac{(-1)^n}{2^{2n-1}} \sum_{l=0}^{n-1} (-1)^l \binom{2n}{l} \cos[2(n-l)y], \quad (73)$$

$$\sin^{2n+1} y = \frac{(-1)^n}{4^n} \sum_{l=0}^n (-1)^l \binom{2n+1}{l} \sin[(2n+1-2l)y]. \quad (74)$$

Due to the orthogonality relations among the trigonometric functions, $I(x)$ only grows without bound if $\sin^k(\beta\xi)$ contains a $\cos \xi$ or $\sin \xi$ term. Eqs. (73) and (74) show that $\sin^k(\beta\xi)$ only contains a term with unit frequency if $\beta = 1/q$ for some integer $q \geq 1$. When this is the case, all terms with $k \geq q$ in Eq. (72) contain a term with unit frequency. Among these terms, the $\sin^q(\beta\xi)$ term has the largest prefactor. Neglecting the other terms with $k > q$, we can evaluate I for any integer multiple m of its period $2\pi q$ to be

$$|I(2\pi m q)| \approx 2\pi m q \left(\frac{\eta^q}{2^q q!} \right). \quad (75)$$

Within each period, $I(x)$ has additional oscillatory behavior due to the other, off-resonance terms in Eq. (72). However, these oscillations are periodic and vanish at every $x = 2\pi m q$,

so they are bounded and do not affect the divergence in Eq. (75). We conclude that $\mathcal{I}(x)$ grows without bound when $\beta = 1/q$, or

$$\bar{\Omega}_e = Nq\Omega_{\text{LK}}. \quad (76)$$

We see that this differs from the **result of the intuitive analysis** [Eq. (68)], as the N -th Fourier harmonic generates infinitely many resonances indexed by $q \geq 1$.

Instead, if β is near but not on a resonance, i.e. $0 < |1 - q\beta| \ll 1$, the amplitude of oscillation of $\mathcal{I}(x)$ is large but bounded. If we take q to be even, then the maximum value of $|\mathcal{I}(x)|$ is dominated by the near-resonance term in Eq. (72),

$$\begin{aligned} |\mathcal{I}(x)| &\simeq \left| \int_0^x \cos \xi \frac{\eta^q}{q!} \frac{1}{2^{q-1}} \cos(q\beta\xi) d\xi \right| \\ &\leq \frac{|\eta|^q}{2^q q!} \frac{1}{|1 - q\beta|}. \end{aligned} \quad (77)$$

If q is instead odd, we use Eq. (74) instead of Eq. (73) and integrate against $i \sin \xi$ instead of $\cos \xi$ in Eq. (72), which results in the same bound on the oscillation amplitude. Returning to Eq. (69), we neglect the first, bounded term ($\lesssim e^\eta \simeq 1$) on the right-hand side and obtain the total oscillation amplitude due to a q -th order resonance with the N -th Fourier harmonic

$$|\Delta \bar{\theta}_e|_{Nq} \sim \frac{1}{2^q q!} \left| \tan \Delta I_{eN} \left[\frac{\Omega_{eN} \cos(\Delta I_{eN})}{N\Omega_{\text{LK}}} \right]^q \left(\frac{\bar{\Omega}_e}{\bar{\Omega}_e - qN\Omega_{\text{LK}}} \right) \right|. \quad (78)$$

Since $\bar{\Omega}_e/N\Omega_{\text{LK}} \approx q$, this reduces to Eq. (68) when $q = 1$, as expected.

2. Generalization to Multiple Fourier Harmonics

After having understood the effect of a single Fourier harmonic, we now return to the **spin evolution equation** containing all of the Fourier harmonics [Eq. (62)]. If $\bar{\Omega}_e/\Omega_{\text{LK}} \approx M$, there can now be multiple N and q satisfying $Nq = M$. By linearity, the total $|\Delta \bar{\theta}_e|$ is given by the sum over all of the resonances, so that

$$|\Delta \bar{\theta}_e| \approx \sum_{N,q|Nq=M} |\Delta \bar{\theta}_e|_{Nq}, \quad (79)$$

where $|\Delta \bar{\theta}_e|_{Nq}$ is given by Eq. (78).

We next attempt to understand whether particular combinations of N and q dominate this sum. We make a few simplifying assumptions: (i) all N harmonics are approximately equal [52], (ii) $\Omega_{eN} \sim \bar{\Omega}_e$ and $\cos \Delta I_{eN} \simeq 1$ (e.g. Figs. 5 and 6). Under these assumptions, $|\Delta \bar{\theta}_e|_{Nq}$ with fixed $Nq = M$ scales with respect to q as

$$|\Delta \bar{\theta}_e|_{Nq} \propto \frac{\cos^q(\Delta I_{eN}) q^q}{2^q q!}. \quad (80)$$

Stirling's **formula** then suggests that $|\Delta \bar{\theta}_e|_{Nq} \propto (\cos(\Delta I_{eN}) e/2)^q / \sqrt{q} \sim 1$. **Thus**, we conclude that all

combinations of N and q satisfying $Nq = M$ result in comparable oscillation amplitudes. For simplicity, we evaluate this amplitude for $q = 1$ and $N = M$. If we denote the number of pairs of N and q satisfying $Nq = M$ by $d(M)$ (the number of positive divisors of M), we can approximate Eq. (79) by:

$$\begin{aligned} |\Delta \bar{\theta}_e| &\approx d(M) |\Delta \bar{\theta}_e|_{M1} \\ &\sim \frac{d(M)}{2} \left| \frac{\Omega_{eM} \sin(\Delta I_{eM})}{\bar{\Omega}_e - M\Omega_{\text{LK}}} \right|, \end{aligned} \quad (81)$$

Note that this agrees with Eq. (68) except for the factor of $d(M)$. Appendix A 3 demonstrates that Eq. (81) is in good agreement with detailed numerical simulations when $M = 1$ or $M = 2$, the two **most** relevant cases for **our study**.

C. Effect of Resonances in LK-Induced Mergers

We first consider the effect of these resonances ($\bar{\Omega}_e = M\Omega_{\text{LK}}$) on the LK-induced regime, using the fiducial parameters (as in Figs. 1 and 2). Numerically, we find that $\bar{\Omega}_e < \Omega_{\text{LK}}$ for the region of parameter space relevant to LK-induced mergers (see Fig. 10), so we focus on the effect of the $M = 1$ resonance. If, for the entire inspiral, $\bar{\Omega}_e < \Omega_{\text{LK}}$ by a sufficient margin that Eq. (81) remains small, then the conservation of $\bar{\theta}_e$ cannot be significantly affected by this resonance. For the fiducial simulation, Fig. 5 shows the ratio $\bar{\Omega}_e/\Omega_{\text{LK}}$ in the middle panel (black) and the amplitude of oscillation of $\bar{\theta}_e$ due to the $M = 1$ resonance [Eq. (81)] in the bottom panel (blue). We see that the system is never close to the resonant condition $\bar{\Omega}_e/\Omega_{\text{LK}} = 1$, and as a result the **net** effect of the resonance never exceeds a few degrees.

For a more precise comparison, the bottom-rightmost panel of Fig. 6 compares $|\Delta \bar{\theta}_e|$ in the fiducial simulation to the expected contributions from nonadiabatic [Eq. (41)] and resonant [Eq. (81) for $M = 1$] effects in the regime where $\mathcal{A} \simeq 1$. We see that Eq. (81) for $M = 1$ describes the oscillations in $\bar{\theta}_e$ very well. The agreement is poorer in the bottom-rightmost panel of Fig. 7, as the nonadiabatic effect is comparatively stronger.

It is somewhat surprising that the contribution of the resonances to the instantaneous $|\Delta \bar{\theta}_e|$ when $\mathcal{A} \simeq 1$ is dominant over that of the nonadiabatic contribution. In **Section IV**, we **have shown** that neglecting resonant terms still allows for an accurate prediction of the final $\bar{\theta}_e$ deviation [Eq. (52)]. This implies that, while the resonances have a larger contribution to $|\Delta \bar{\theta}_e|$, the nonadiabatic effect is more important in determining $|\Delta \bar{\theta}_e|_f$. This also requires that a $|\Delta \bar{\theta}_e|$ of up to a few degrees due to resonant effects not affect $|\Delta \bar{\theta}_e|_f$ by more than $\sim 0.01^\circ$. This differs from the nonadiabatic case, where we find $|\Delta \bar{\theta}_e|_f \sim \max |\Delta \bar{\theta}_e|$. The origin of these differences in behaviors may be due to the complex phases cancelling differently in Eqs. (40) and (69) as the BH binary coalesces.

D. Effect of Resonances in LK-Enhanced Mergers

We turn now to the case of LK-enhanced mergers, as was studied in LL17, where the inner binary is sufficiently compact

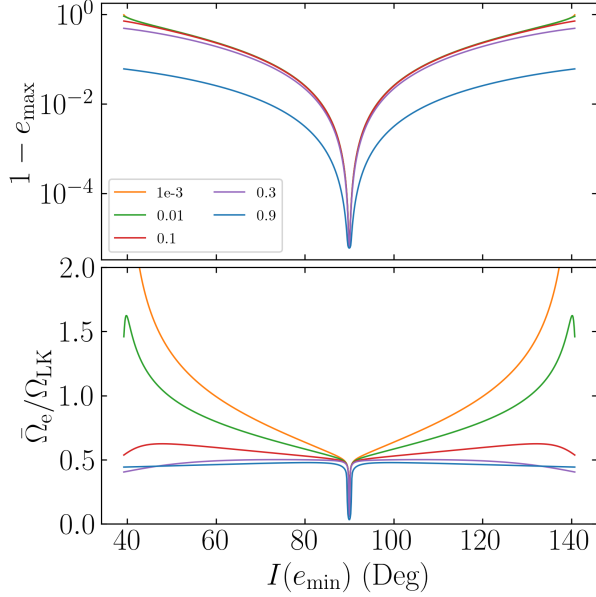


FIG. 10. e_{\max} and $\bar{\Omega}_e/\Omega_{\text{LK}}$ as a function of $I(e_{\min})$, the inclination of the inner binary at eccentricity minimum, for varying values of e_{\min} (different colors as labeled) for a LK-induced merger (with the parameters the same as in Figs. 1 and 2). In this case, only systems with I_0 close to 90° will merge within a Hubble time, $I(e_{\min}) \sim 90^\circ$ for most of the evolution (see Fig. 1) until $e_{\min} \approx 1$ is satisfied. This plot shows that $\bar{\Omega}_e \lesssim 0.5\Omega_{\text{LK}}$ is a general feature of LK-induced mergers, as is the case for the fiducial simulation (see Fig. 5).

(~ 0.1 AU) that it can merge in isolation via GW radiation. We consider a set of parameters that has the same $t_{\text{LK},0}$ as the system studied in LL17 but has a tertiary SMBH: $m_1 = m_2 = 30M_\odot$, $a_0 = 0.1$ AU, $e_0 = 10^{-3}$, $m_3 = 3 \times 10^7 M_\odot$, $\tilde{a}_{\text{out}} = 300$ AU, and $e_{\text{out}} = 0$. We show that the resonances studied above play an important role in shaping the $\theta_{\text{sl},f}$ distribution for this regime.

First, we illustrate the $\theta_{\text{sl},f}$ distribution obtained via numerical simulation, shown as the blue dots in Fig. 11. The prediction assuming **adiabatic invariance (i.e. the conservation of $\bar{\theta}_e$)** is shown in the red solid line. Good agreement is observed both when no eccentricity excitation occurs ($I_0 \lesssim 50^\circ$ and $I_0 \gtrsim 130^\circ$) and when $|\mathcal{A}| \gg 1$ ($80^\circ \lesssim I_0 \lesssim 100^\circ$). However, we see in Fig. 11 that for intermediate inclinations, $I_0 \in [50, 80]$ and $I_0 \in [100, 130]$, $\theta_{\text{sl},f}$ varies over a large range and does not agree with the prediction of $\bar{\theta}_e$ conservation. Note that these inclinations correspond to neither the fastest nor slowest merging systems.

We attribute the origin of this wide scatter to resonance interactions. Fig. 12 illustrates that **for these intermediate inclinations, the condition $\bar{\Omega}_e \sim \Omega_{\text{LK}}$ is satisfied**. In addition, as the inner binary coalesces under GW radiation, e_{\min} becomes larger (e.g. see Fig. 1). This causes the locations of the resonances **at inclinations less than (greater than) $I = 90^\circ$ to evolve to smaller (larger) inclinations**. As the location of the resonances is a sensitive function of e_{\min} , resonance passage is

nonadiabatic. Thus, we expect that all systems that encounter the resonance, i.e. all systems with intermediate initial inclinations, will experience an impulsive kick to $\bar{\theta}_e$, resulting in poor $\bar{\theta}_e$ conservation. This result is denoted by the **two** red shaded regions in Fig. 11.

While the outer edges of the red shaded regions described above are located at the critical I_0 required for nonzero eccentricity excitation, the inner edges are harder to characterize. Systems with initial inclinations close to 90° start at the edge of the $M = 1$ resonance and quickly evolve **away** from it (as e_{\min} increases and a decreases). As such, they only interact briefly and weakly with the resonances, and the cumulative effect of the resonance interaction can be estimated by evaluating Eq. (81) for $M = 1$ at the initial conditions. We empirically choose the transition between such “weakly” and “strongly” resonant systems, i.e. the inner edge of the broad red shaded region in Fig. 11, when the oscillation semi-amplitude $|\Delta\bar{\theta}_e|$ predicted by Eq. (81) exceeds 3° .

To understand the general characteristics of systems that interact strongly with resonances, we examine the quantities in Eq. (81):

- $\sin(\Delta I_{eN})$ is small unless $\mathcal{A} \approx 1$. Otherwise, $\mathbf{\Omega}_e$ does not nutate substantially within a LK cycle, and all the $\mathbf{\Omega}_{eN}$ are aligned with $\bar{\mathbf{\Omega}}_e$ which implies that the $\Delta I_{eN} \approx 0$ for all $N \geq 1$.
- Smaller values of e_{\min} increase $\bar{\Omega}_e/\Omega_{\text{LK}}$, as shown in Fig. 12.

However, the timescales over which \mathcal{A} increases and e_{\min} decreases are comparable (see Fig. 1). This implies that, if $\mathcal{A} \ll 1$ initially, which is the case for LK-induced mergers, then e_{\min} will be very close to unity when \mathcal{A} grows to be ≈ 1 , and the contribution predicted by Eq. (81) will remain small throughout the entire evolution. On the other hand, only if $\mathcal{A} \approx 1$ and $e_{\min} \ll 1$ initially, as is the case for the intermediate inclinations in the LK-enhanced regime, are resonant interactions likely to be significant.

VI. STELLAR MASS BLACK HOLE TRIPLES

In this section, we extend our predictions for the final spin-orbit misalignment angle $\theta_{\text{sl},f}$ to systems where all three masses are comparable and the ratio of the angular momenta of the two binaries, given by

$$\eta \equiv \frac{L}{L_{\text{out}}}\bigg|_{e=e_{\text{out}}=0} = \frac{\mu}{\mu_{\text{out}}} \left[\frac{m_{12}a}{m_{123}a_{\text{out}}} \right]^{1/2}, \quad (82)$$

where $m_{123} = m_{12} + m_3$ and $\mu_{\text{out}} = m_{12}m_3/m_{123}$, is not negligible. When $\eta \neq 0$, \mathbf{L}_{out} is no longer fixed, but the total angular momentum $\mathbf{L}_{\text{tot}} \equiv \mathbf{L} + \mathbf{L}_{\text{out}}$ is fixed. We choose the coordinate system with $\hat{\mathbf{Z}} = \hat{\mathbf{L}}_{\text{tot}}$, shown in Fig. 13.

To analyze this system, we still assume $e_{\text{out}} \ll 1$ so that the octupole-order effects are negligible. To calculate the evolution of \mathbf{L} , it is only necessary to evolve the orbital elements of the inner binary [a , e , δ , I_{tot} (its inclination relative to $\hat{\mathbf{L}}_{\text{tot}}$),

and ω] and a single orbital element for the outer binary, its inclination $I_{\text{tot,out}}$ relative to $\hat{\mathbf{L}}_{\text{tot}}$. The equations of motion are given by [41]:

$$\frac{da}{dt} = \left(\frac{da}{dt} \right)_{\text{GW}}, \quad (83)$$

$$\frac{de}{dt} = \frac{15}{8t_{\text{LK}}} e j(e) \sin 2\omega \sin^2 I + \left(\frac{de}{dt} \right)_{\text{GW}}, \quad (84)$$

$$\frac{d\varphi}{dt} = \frac{L_{\text{tot}}}{L_{\text{out}}} \frac{3}{4t_{\text{LK}}} \frac{\cos I (5e^2 \cos^2 \omega - 4e^2 - 1)}{j(e)}, \quad (85)$$

$$\frac{dI_{\text{tot}}}{dt} = -\frac{15}{16t_{\text{LK}}} \frac{e^2 \sin 2\omega \sin 2I}{j(e)}, \quad (86)$$

$$\frac{dI_{\text{tot,out}}}{dt} = -\eta \frac{15}{8t_{\text{LK}}} \left(e^2 \sin 2\omega \sin I \right), \quad (87)$$

$$\frac{d\omega}{dt} = \frac{3}{t_{\text{LK}}} \left\{ \frac{4 \cos^2 I + (5 \cos(2\omega) - 1)(1 - e^2 - \cos^2 I)}{8j(e)} + \frac{\eta \cos I}{8} [2 + e^2(3 - 5 \cos(2\omega))] \right\} + \Omega_{\text{GR}}, \quad (88)$$

where $I = I_{\text{tot}} + I_{\text{tot,out}}$ is the relative inclination between the two angular momenta. The spin evolution of one of the inner BHs is then described in the frame corotating with \mathbf{L} about \mathbf{L}_{tot} by the equation of motion

$$\left(\frac{d\mathbf{S}}{dt} \right)_{\text{rot}} = \mathbf{\Omega}_e \times \mathbf{S}, \quad (89)$$

where

$$\mathbf{\Omega}_e \equiv \Omega_{\text{SL}} \hat{\mathbf{L}} + \Omega_{\text{L}} \hat{\mathbf{L}}_{\text{tot}}. \quad (90)$$

where $\Omega_{\text{L}} = -d\varphi/dt$ [Eq. (85)] is the rate of precession of \mathbf{L} about \mathbf{L}_{tot} . **As in Section IV, we consider the LK-averaged $\mathbf{\Omega}_e$ and neglect the harmonic terms:**

$$\left(\frac{d\bar{\mathbf{S}}}{dt} \right)_{\text{rot}} = \bar{\mathbf{\Omega}}_e \times \bar{\mathbf{S}}, \quad (91)$$

where

$$\begin{aligned} \bar{\mathbf{\Omega}}_e &= \overline{\Omega_{\text{SL}} \sin I_{\text{tot}}} \hat{\mathbf{X}} + \left(\overline{\Omega_{\text{L}}} + \overline{\Omega_{\text{SL}} \cos I_{\text{tot}}} \right) \hat{\mathbf{Z}} \\ &\equiv \overline{\Omega_{\text{SL}}} \sin \bar{I}_{\text{tot}} \hat{\mathbf{X}} + \left(\overline{\Omega_{\text{L}}} + \overline{\Omega_{\text{SL}} \cos \bar{I}_{\text{tot}}} \right) \hat{\mathbf{Z}}. \end{aligned} \quad (92)$$

The results of Section IV suggest that the angle $\bar{\theta}_e$ is an adiabatic invariant, where $\bar{\theta}_e$ is given by

$$\cos \bar{\theta}_e \equiv \frac{\bar{\Omega}_e}{\Omega_e} \cdot \bar{\mathbf{S}}, \quad (93)$$

where $\bar{\mathbf{S}}$ is the spin vector averaged over a LK cycle. The orientation of $\bar{\mathbf{\Omega}}_e$ is described by the inclination angle $\bar{I}_{\text{tot,e}}$ (Fig. 13), which can be expressed using Eq. (92)

$$\tan \bar{I}_{\text{tot,e}} = \frac{\mathcal{A} \sin \bar{I}_{\text{tot}}}{1 + \mathcal{A} \cos \bar{I}_{\text{tot}}}, \quad (94)$$

where $\mathcal{A} \equiv \overline{\Omega_{\text{SL}}}/\overline{\Omega_{\text{L}}}$ is the adiabaticity parameter.

At $t = t_f$, the inner binary is sufficiently compact that θ_{sl} is frozen (see bottom right panel of Fig. 1), and the system satisfies $\mathcal{A} \gg 1$ ($\overline{\Omega_{\text{SL}}} \propto a^{-5/2}$ while $\overline{\Omega_{\text{L}}} \propto a^{3/2}$). When this is the case, $\bar{\mathbf{\Omega}}_e \parallel \mathbf{L}$, and so $\bar{\theta}_{e,f} = \theta_{\text{sl},f}$. Then, since adiabatic invariance implies $\bar{\theta}_{e,f} = \bar{\theta}_{e,0}$,

$$\theta_{\text{sl},f} = \bar{\theta}_{e,0}. \quad (95)$$

We first consider the case where $\mathbf{S}_0 \propto \mathbf{L}_0$. Then $\bar{\theta}_{e,0} = |I_{\text{tot},0} - \bar{I}_{\text{tot,e},0}|$ (see Fig. 13), and so

$$\theta_{\text{sl},f} = |I_{\text{tot},0} - \bar{I}_{e,0}|. \quad (96)$$

Suppose additionally that the binary initially satisfies $|\overline{\Omega_{\text{L}}}| \gg \overline{\Omega_{\text{SL}}}$, then $\bar{\mathbf{\Omega}}_e$ is either parallel or anti-parallel to \mathbf{L}_{tot} depending on whether $\overline{\Omega_{\text{L}}}$ is positive or negative. We denote the starting mutual inclination for which $\overline{\Omega_{\text{L}}}$ changes sign by I_c . Note that $I_c > 90^\circ$: even though Ω_{L} changes sign at $I_0 = 90^\circ$, the inclination decreases over a LK cycle for $I < I_{\text{lim}}$ (where $I_{\text{lim}} > 90^\circ$ is the starting mutual inclination that maximizes e_{max} [31]), so the sign of Ω_{L} changes over a LK cycle for some $I_c \in (90^\circ, I_{\text{lim}})$. We then obtain that

$$\theta_{\text{sl},f} = \begin{cases} I_{\text{tot},0}, & I_0 < I_c, \\ 180^\circ - I_{\text{tot},0}, & I_0 > I_c. \end{cases} \quad (97)$$

More generally, so long as $\mathcal{A} \ll 1$ initially, we can specify the initial spin orientation by $\theta_{s,\text{tot},0}$, the initial angle between \mathbf{S} and \mathbf{L}_{tot} , giving

$$\theta_{\text{sl},f} = \begin{cases} \theta_{s,\text{tot},0}, & I < I_c, \\ 180^\circ - \theta_{s,\text{tot},0}, & I > I_c. \end{cases} \quad (98)$$

We first compare these results to numerical simulations by considering a stellar-mass BH triple that is in the LK-induced regime: we use the same inner binary parameters as the **example of Fig. 1, but for** a tertiary companion with $m_3 = 30M_\odot$, $a_{\text{out}} = 4500$ AU, and $e_{\text{out}} = 0$. Fig. 14 shows that Eq. (96) accurately predicts $\theta_{\text{sl},f}$ when $\theta_{\text{sl},0} = 0^\circ$ for this parameter regime when conservation of $\bar{\theta}_e$ is good. Furthermore, deviations from exact $\bar{\theta}_e$ conservation are well described by Eq. (61), the prediction of the theory in Section IV. Unlike the $\eta = 0$ case (Fig. 2), $\theta_{\text{sl},f}$ is not symmetric about $I_c \approx 92.14^\circ$. This is because $|\overline{\Omega_{\text{L}}}|$ is not exactly equal on either side of I_c . Additionally, unlike in the $\eta = 0$ case, the minimum $\theta_{\text{sl},f}$ is not exactly zero. We showed in Section IV D that when $\eta = 0$, \mathbf{L} is fixed when $I_0 = 90^\circ$, as $d\varphi/dt = dI/dt = 0$. For nonzero η , **neither $d\varphi/dt$ nor dI_{tot}/dt is zero at $I_0 = I_c$.**

Eq. (96) also gives good agreement in the LK-enhanced merger regime. We consider the same inner binary parameters as in Fig. 11 but use a tertiary companion with $m_3 = 30M_\odot$, $a_{\text{out}} = 3$ AU, and $e_{\text{out}} = 0$. The results are shown in Fig. 15.

VII. CONCLUSION AND DISCUSSION

In this paper, we have carried out **a** theoretical study on the evolution of spin-orbit misalignments in tertiary-induced

black-hole (BH) binary mergers. Recent numerical works [30, 31, 39, 40, 50] have revealed that when binary BHs undergo mergers due to Lidov-Kozai (LK) oscillations driven by a tertiary companion, the BH spin may evolve toward a perpendicular state where the final spin-orbit misalignment angle θ_{sl} is close to 90° . Our theoretical analysis in this paper provides an understanding of this “ 90° attractor” and characterizes its regime of validity and various spin evolution behaviors during **such** LK-induced mergers. We focus on hierarchical triple systems where the inner BH binary experiences the “standard” quadrupole LK oscillations and eventually merges, with the octupole effects playing a negligible role [$\epsilon_{oct} \ll 1$; see Eq. (14)]. For such systems, the spin vectors of the inner BHs obey a simple evolution equation, Eq. (22) or Eq. (91), where the “effective” precession rate Ω_e varies quasi-periodically due to the combined effects of LK oscillations and gravitational radiation. Analysis of this equation yields the following conclusions:

- For BH binaries that have too large initial separations to merge **in isolation**, LK-induced mergers require large/extreme eccentricity excitations in the binary driven by a highly inclined tertiary companion. For such systems, the BH spin evolution behavior can be generally captured by replacing Ω_e with its LK-average $\bar{\Omega}_e$ (thus neglecting the **Fourier harmonics**). If the orbital decay is sufficiently gradual, the angle $\bar{\theta}_e$ [Eq. (36)] between the spin axis and $\bar{\Omega}_e$ is an adiabatic invariant. This naturally explains the “ 90° attractor” for the final spin-orbit misalignment angle when the initial tertiary inclination I_0 is not too close to 90° and the initial BH spin axis is aligned with the orbital angular momentum axis (see Fig. 2). We show that the deviation from perfect adiabaticity can be predicted from initial conditions [see Eq. 52 and Fig. 9].
- When the resonant condition $\bar{\Omega}_e \approx M\Omega_{LK}$ for integer M is satisfied, significant variations in $\bar{\theta}_e$ can arise. We derive an analytic estimate of this variation amplitude [Eq. (81)]. This estimate demonstrates that the resonances are unimportant for “LK-induced” mergers (see above), but become important for “LK-enhanced” mergers, where the BH binaries exhibit only modest eccentricity excitations. Our analysis of the resonance effects qualitatively explain the behavior in $\theta_{sl,f}$ as seen in LK-enhanced mergers (see Figs. 11 and 15).
- For LK-induced mergers of BH binaries with general tertiary companions, we provide an analytic prescription for calculating the final spin-orbit misalignment angle for arbitrary initial spin orientations (Section VI). This prescription is based on the approximate adiabatic invariance of $\bar{\theta}_e$, and produces results that are in agreement with numerical simulations (see Fig. 14) in the

appropriate regime.

There are several simplifications in our theoretical analysis that are worth remembering. (i) We have neglected the octupole effects in the LK oscillations. This is appropriate for systems where the tertiary orbit is **not** eccentric, **when** the semi-major axis a_{out} is much larger than the inner binary (as in the case when the tertiary is a SMBH), or **when** the inner binary BHs have nearly equal masses. The octupole effects are known to significantly broaden the inclination window for extreme eccentricity excitations, and therefore enhance the efficiency of LK-induced mergers [31]. The octupole-order LK effect is not integrable, and the eccentricity excitations are no longer regular. As a result, when the octupole effects are important, Ω_e has neither consistent direction nor magnitude, and our theory cannot be applied. In fact, the resulting $\theta_{sl,f}$ distribution is largely unrelated to the initial $\bar{\theta}_{e,0}$ [31], and no “ 90° attractor” is expected [31]. (ii) If the system is not sufficiently hierarchical (a_{out} is too small), the double averaging approximation for the dynamics of the triple breaks down [31]. In this case, there is little reason to expect any relation between $\theta_{sl,f}$ and $\bar{\theta}_{e,0}$. However, Liu and Lai [31] found that the double averaged equations predict the correct merger window and merger fractions even beyond their regime of validity if the octupole effect is weak, so it is possible that our results concerning $\theta_{sl,f}$ are also somewhat robust even when the double averaged equations formally break down. (iii) In this work, we only consider spin-orbit coupling, and follow the evolution of θ_{sl} until the orbital separation is sufficiently small that the inner binary is gravitationally decoupled from the tertiary and the spin-orbit misalignment angle is frozen. To leading post-Newtonian (PN) order, θ_{sl} is constant for small separations until the spin-spin interaction (2 PN) becomes important. This interaction is non-negligible only when binary enters the LIGO band and when the spin magnitude of each is appreciable [39, 50].

As noted in Section I, the merging BH binaries detected by LIGO in O1 and O2 have $\chi_{eff} \sim 0$ [1, 2]. One possible explanation for this is that BHs are born slowly rotating [e.g. 53]. But our “ 90° attractor” provides an alternative explanation with no assumptions on the BH spin magnitudes if the mergers are “LK-induced” and $\theta_{sl,0} \approx 0^\circ$. In the O3 event GW190521, each BH has a significant spin magnitude and a large spin-orbit misalignment angle [38]. If the evolution history of the system resembled our LK-induced scenario, a primordial $\theta_{sl,0} \approx 0^\circ$ would be consistent with the observed outcome.

VIII. ACKNOWLEDGEMENTS

This work has been supported in part by the NSF grant AST-17152. YS is supported by the NASA FINESST grant 19-ASTRO19-0041.

[1] B. P. Abbott, R. Abbott, T. Abbott, M. Abernathy, F. Acernese, K. Ackley, C. Adams, T. Adams, P. Addesso, R. Adhikari, *et al.*,

- [2] B. Abbott, R. Abbott, T. Abbott, S. Abraham, F. Acernese, K. Ackley, C. Adams, R. Adhikari, V. Adya, C. Affeldt, *et al.*, The Astrophysical Journal Letters **882**, L24 (2019).
- [3] V. Lipunov, K. Postnov, and M. Prokhorov, Astronomy Letters **23**, 492 (1997).
- [4] V. Lipunov, V. Kornilov, E. Gorbovskoy, D. Buckley, N. Tiurina, P. Balanutsa, A. Kuznetsov, J. Greiner, V. Vladimirov, D. Vlasenko, *et al.*, Monthly Notices of the Royal Astronomical Society **465**, 3656 (2017).
- [5] P. Podsiadlowski, S. Rappaport, and Z. Han, Monthly Notices of the Royal Astronomical Society **341**, 385 (2003).
- [6] K. Belczynski, M. Dominik, T. Bulik, R. O’Shaughnessy, C. Fryer, and D. E. Holz, The Astrophysical Journal Letters **715**, L138 (2010).
- [7] K. Belczynski, D. E. Holz, T. Bulik, and R. O’Shaughnessy, Nature **534**, 512 (2016).
- [8] M. Dominik, K. Belczynski, C. Fryer, D. E. Holz, E. Berti, T. Bulik, I. Mandel, and R. O’Shaughnessy, The Astrophysical Journal **759**, 52 (2012).
- [9] M. Dominik, K. Belczynski, C. Fryer, D. E. Holz, E. Berti, T. Bulik, I. Mandel, and R. O’Shaughnessy, The Astrophysical Journal **779**, 72 (2013).
- [10] M. Dominik, E. Berti, R. O’Shaughnessy, I. Mandel, K. Belczynski, C. Fryer, D. E. Holz, T. Bulik, and F. Pannarale, The Astrophysical Journal **806**, 263 (2015).
- [11] K. Postnov and A. Kuranov, Monthly Notices of the Royal Astronomical Society **483**, 3288 (2019).
- [12] K. Belczynski, J. Klencki, C. Fields, A. Olejak, E. Berti, G. Meynet, C. Fryer, D. Holz, R. O’Shaughnessy, D. Brown, *et al.*, Astronomy & Astrophysics **636**, A104 (2020).
- [13] S. F. P. Zwart and S. L. McMillan, The Astrophysical Journal Letters **528**, L17 (1999).
- [14] R. M. O’leary, F. A. Rasio, J. M. Fregeau, N. Ivanova, and R. O’Shaughnessy, The Astrophysical Journal **637**, 937 (2006).
- [15] M. C. Miller and V. M. Lauburg, The Astrophysical Journal **692**, 917 (2009).
- [16] S. Banerjee, H. Baumgardt, and P. Kroupa, Monthly Notices of the Royal Astronomical Society **402**, 371 (2010).
- [17] J. Downing, M. Benacquista, M. Giersz, and R. Spurzem, Monthly Notices of the Royal Astronomical Society **407**, 1946 (2010).
- [18] B. M. Ziosi, M. Mapelli, M. Branchesi, and G. Tormen, Monthly Notices of the Royal Astronomical Society **441**, 3703 (2014).
- [19] C. L. Rodriguez, M. Morscher, B. Pattabiraman, S. Chatterjee, C.-J. Haster, and F. A. Rasio, Physical Review Letters **115**, 051101 (2015).
- [20] J. Samsing and E. Ramirez-Ruiz, The Astrophysical Journal Letters **840**, L14 (2017).
- [21] J. Samsing and D. J. D’Orazio, Monthly Notices of the Royal Astronomical Society **481**, 5445 (2018).
- [22] C. L. Rodriguez, P. Amaro-Seoane, S. Chatterjee, and F. A. Rasio, Physical Review Letters **120**, 151101 (2018).
- [23] L. Gondán, B. Kocsis, P. Raffai, and Z. Frei, The Astrophysical Journal **860**, 5 (2018).
- [24] O. Blaes, M. H. Lee, and A. Socrates, The Astrophysical Journal **578**, 775 (2002).
- [25] M. C. Miller and D. P. Hamilton, The Astrophysical Journal **576**, 894 (2002).
- [26] L. Wen, The Astrophysical Journal **598**, 419 (2003).
- [27] F. Antonini and H. B. Perets, The Astrophysical Journal **757**, 27 (2012).
- [28] F. Antonini, S. Toonen, and A. S. Hamers, The Astrophysical Journal **841**, 77 (2017).
- [29] K. Silsbee and S. Tremaine, The Astrophysical Journal **836**, 39 (2017).
- [30] B. Liu and D. Lai, The Astrophysical Journal Letters **846**, L11 (2017).
- [31] B. Liu and D. Lai, The Astrophysical Journal **863**, 68 (2018).
- [32] L. Randall and Z.-Z. Xianyu, The Astrophysical Journal **853**, 93 (2018).
- [33] B.-M. Hoang, S. Naoz, B. Kocsis, F. A. Rasio, and F. Dosopoulou, The Astrophysical Journal **856**, 140 (2018).
- [34] P. Schmidt, F. Ohme, and M. Hannam, Physical Review D **91**, 024043 (2015).
- [35] B. Zackay, T. Venumadhav, L. Dai, J. Roulet, and M. Zaldarriaga, Physical Review D **100**, 023007 (2019).
- [36] T. Venumadhav, B. Zackay, J. Roulet, L. Dai, and M. Zaldarriaga, Physical Review D **101**, 083030 (2020).
- [37] B. P. Abbott, R. Abbott, T. Abbott, M. Abernathy, F. Acernese, K. Ackley, C. Adams, T. Adams, P. Addesso, R. Adhikari, *et al.*, Physical Review D **102**, 043015 (2020).
- [38] R. Abbott, T. Abbott, S. Abraham, F. Acernese, K. Ackley, C. Adams, R. Adhikari, V. Adya, C. Affeldt, M. Agathos, *et al.*, The Astrophysical Journal Letters **900**, L13 (2020).
- [39] B. Liu, D. Lai, and Y.-H. Wang, The Astrophysical Journal **881**, 41 (2019).
- [40] F. Antonini, C. L. Rodriguez, C. Petrovich, and C. L. Fischer, Monthly Notices of the Royal Astronomical Society: Letters **480**, L58 (2018).
- [41] B. Liu, D. J. Muñoz, and D. Lai, Monthly Notices of the Royal Astronomical Society **447**, 747 (2015).
- [42] K. R. Anderson, N. I. Storch, and D. Lai, Monthly Notices of the Royal Astronomical Society **456**, 3671 (2016).
- [43] H. Kinoshita, Celestial Mechanics and Dynamical Astronomy **57**, 359 (1993).
- [44] N. I. Storch and D. Lai, Monthly Notices of the Royal Astronomical Society **448**, 1821 (2015).
- [45] N. I. Storch, K. R. Anderson, and D. Lai, Science **345**, 1317 (2014).
- [46] N. I. Storch, D. Lai, and K. R. Anderson, Monthly Notices of the Royal Astronomical Society **465**, 3927 (2017).
- [47] G. Floquet, in *Annales scientifiques de l’École normale supérieure*, Vol. 12 (1883) pp. 47–88.
- [48] C. Chicone, *Ordinary differential equations with applications*, Vol. 34 (Springer Science & Business Media, 2006).
- [49] More formally, $\tilde{\mathbf{M}} = \tilde{\Phi}(P_{LK})$ where $\tilde{\Phi}(t)$ is the *principal fundamental matrix solution*: the columns of $\tilde{\Phi}$ are solutions to Eq. (22) and $\tilde{\Phi}(0)$ is the identity. By linearity, the columns of $\tilde{\Phi}(t)$ remain orthonormal, while its determinant does not change, so $\tilde{\mathbf{M}}$ is a proper orthogonal matrix, or a rotation matrix.
- [50] H. Yu, S. Ma, M. Giesler, and Y. Chen, arXiv preprint arXiv:2007.12978 (2020).
- [51] D. Zwillinger, *CRC standard mathematical tables and formulae* (CRC press, 2002).
- [52] This approximation is suitable for the problem studied in the main text because the only characteristic frequency scale is $j_{\min}^{-1} \gg 1$, so all Fourier harmonics Ω_{eN} for $N \lesssim j_{\min}^{-1}$ are similar.
- [53] J. Fuller and L. Ma, The Astrophysical Journal Letters **881**, L1 (2019).
- [54] W. Magnus, Communications on pure and applied mathematics **7**, 649 (1954).

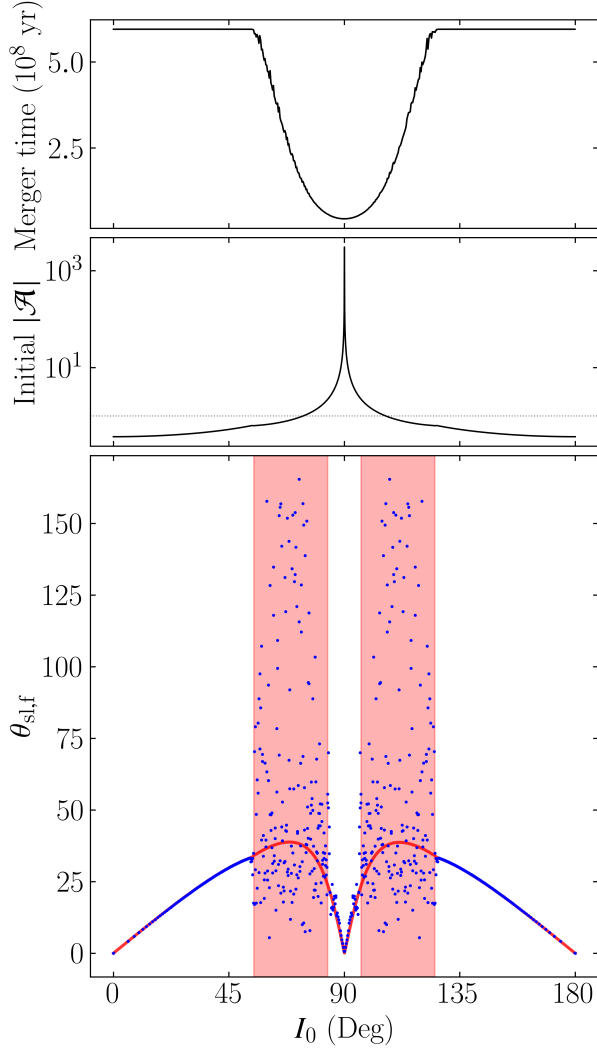


FIG. 11. The merger time (top), the magnitude of the **initial** adiabaticity parameter $|\mathcal{A}| \equiv \bar{\Omega}_{\text{SL}}/|\bar{\Omega}_L|$ (middle), and the final spin-orbit misalignment angle $\theta_{\text{sl},f}$ (bottom) for LK-enhanced **mergers**, with $m_1 = m_2 = 30M_\odot$, $m_3 = 3 \times 10^7 M_\odot$, $a_0 = 0.1$ AU, $e_0 = 10^{-3}$, $\tilde{a}_{\text{out}} = 300$ AU, and $e_{\text{out}} = 0$. In the middle panel, the horizontal dashed line indicates $|\mathcal{A}| = 1$. In the bottom panel, the blue dots denote results from numerical simulations with $\theta_{\text{sl},0} = 0$ [these are symmetric about $I_0 = 90^\circ$, as the equations of motion (3–7) are as well]. The prediction for $\theta_{\text{sl},f}$ assuming conservation of $\bar{\theta}_e$ is shown as the red line, which agrees well with the data both when there is no eccentricity excitation ($I_0 \lesssim 50^\circ$ and $I_0 \gtrsim 130^\circ$) and when $|\mathcal{A}| \gg 1$. For a substantial range of intermediate inclinations ($I_0 \in [50^\circ, 80^\circ]$ and $I_0 \in [100^\circ, 130^\circ]$), $\theta_{\text{sl},f}$ is significantly affected by the resonances as they evolve (see Fig. 12). As such, these initial inclinations are expected to **give rise to a wide range of $\theta_{\text{sl},f}$** , and we denote this with broad red shaded regions.

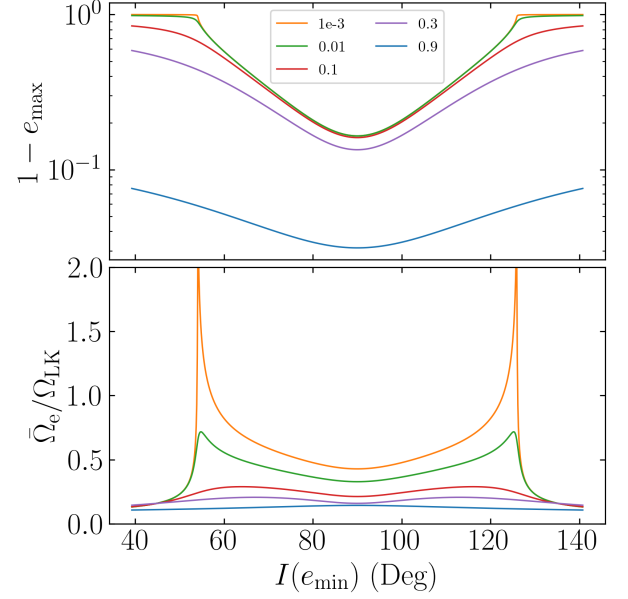


FIG. 12. Same as Fig. 10, but for a LK-enhanced merger (with the parameters of Fig. 11). In the LK-enhanced regime, all initial inclinations merge within a Hubble time, and it is clear that $\bar{\Omega}_e \approx \bar{\Omega}_{\text{LK}}$ can be satisfied for a wide range of initial inclinations **when the initial eccentricity is sufficiently small**.

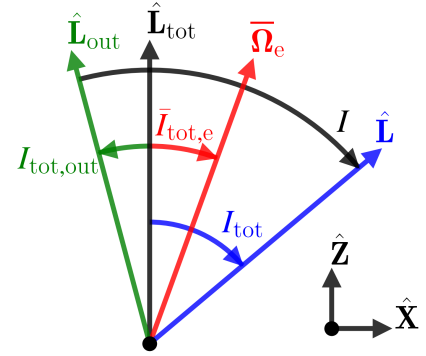


FIG. 13. Definition of angles in the case where L/L_{out} is nonzero. Similar to before, we choose the convention where $I_{\text{tot,e}} \in [0^\circ, 90^\circ]$ when $\bar{\Omega}_L > 0$ and $I_{\text{tot,e}} \in [90^\circ, 180^\circ]$ when $\bar{\Omega}_L < 0$. Here, \mathbf{L}_{out} is not fixed, but $\mathbf{L}_{\text{tot}} \equiv \mathbf{L} + \mathbf{L}_{\text{out}}$ is. Note that the coordinate system is now oriented with $\hat{\mathbf{z}} \propto \mathbf{L}_{\text{tot}}$.

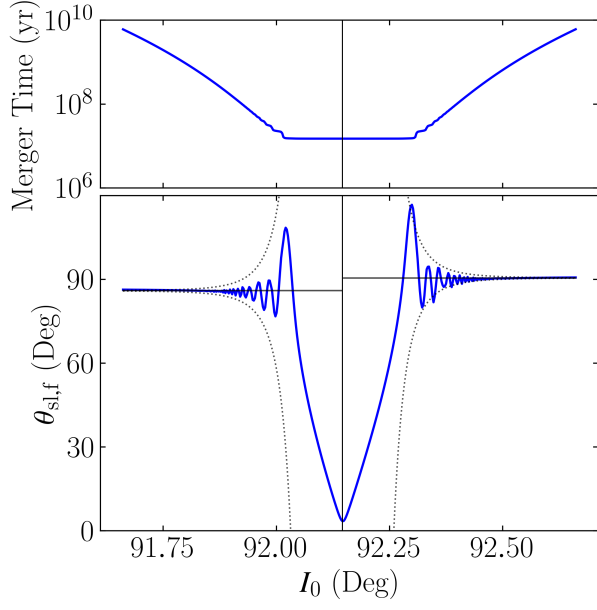


FIG. 14. Similar to Fig. 2 but for stellar-mass tertiary $m_3 = 30M_\odot$ and $\tilde{a}_3 = 4500$ AU. The vertical black line denotes $I_c \approx 92.14^\circ$, the initial inclination for which $\tilde{\Omega}_L$ changes signs, and the two horizontal lines denote the predictions of Eq. (96). The dotted black lines bound the deviation due to non-adiabatic evolution, given by Eq. (61).

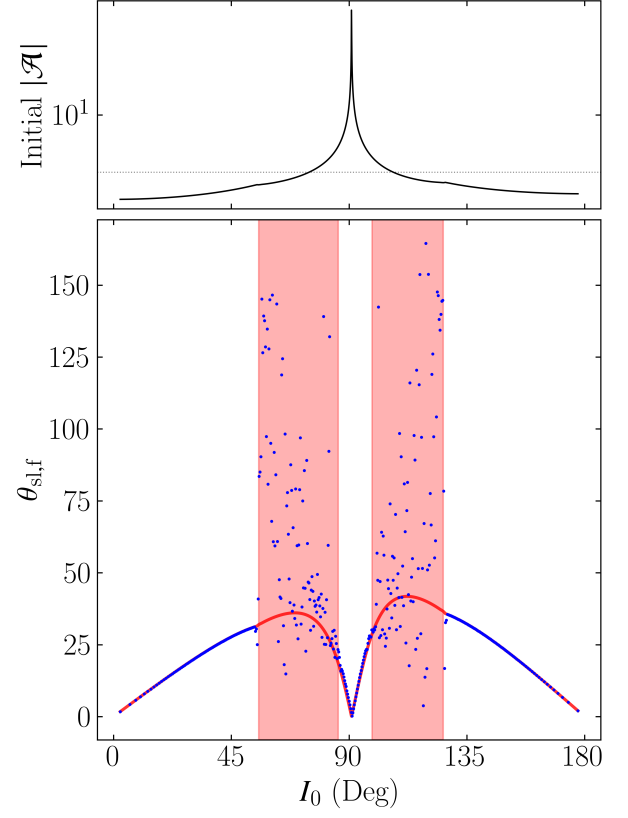


FIG. 15. Similar to Fig. 11 except for a stellar mass tertiary $m_3 = 30M_\odot$ and $\tilde{a}_{\text{out}} = 3$ AU.

Appendix A: Floquet Theory Analysis

In this appendix, we provide an alternative approach to analyzing the BH spin dynamics based on Floquet theory [48] that provides results complementary to those in the main text. Though the resulting equations cannot be analytically solved, they place strong constraints on the allowed behavior of the system. Additionally, Eq. (81) has a natural interpretation in this formulation, and its accuracy is numerically tested in Appendix A 3. We again work in the corotating frame and neglect GW dissipation, so the equation of motion is given by Eq. (22). If we define the matrix operator satisfying $\tilde{\mathbf{A}}\mathbf{S} = \mathbf{\Omega}_e \times \mathbf{S}$, then the equation of motion is

$$\left(\frac{d\mathbf{S}}{dt}\right)_{\text{rot}} = \tilde{\mathbf{A}}\mathbf{S}. \quad (\text{A1})$$

Here, $\tilde{\mathbf{A}}$ is periodic with period T_{LK} .

1. Without Nutation

First, for simplicity, let us assume that $\mathbf{\Omega}_e$ does not nutate, so its orientation is fixed. In this case, Eq. (A1) admits an exact conserved quantity:

$$\frac{d}{dt} [e^{-\Phi}\mathbf{S}] = 0, \quad (\text{A2})$$

where

$$\Phi(t) \equiv \int_0^t \tilde{\mathbf{A}} dt. \quad (\text{A3})$$

Separately, since Eq. (A1) is linear and has periodic coefficients, Floquet theory tells us that $\mathbf{S}(t + T_{\text{LK}})$ is related to $\mathbf{S}(t)$ by the monodromy matrix $\tilde{\mathbf{M}}$:

$$\mathbf{S}(t + T_{\text{LK}}) = \tilde{\mathbf{M}}\mathbf{S}(t). \quad (\text{A4})$$

Comparing Eqs. (A2) and (A4), we immediately find that

$$\begin{aligned} \tilde{\mathbf{M}} &= \exp \left[\int_0^{T_{\text{LK}}} \tilde{\mathbf{A}} dt \right], \\ &= \exp \left[T_{\text{LK}} \bar{\tilde{\mathbf{A}}} \right], \end{aligned} \quad (\text{A5})$$

where again the overline denotes time averaging. As $\tilde{\mathbf{M}}$ is a rotation matrix, call \mathbf{R} its rotation axis, or its eigenvector with eigenvalue 1. But $\mathbf{R} = \hat{\mathbf{\Omega}}_e$, so $\mathbf{S} \cdot \hat{\mathbf{\Omega}}_e$ must be constant for every $t = NT_{\text{LK}}$.

This example is somewhat trivial, as if $\mathbf{\Omega}_e$ does not nutate, then \mathbf{S} just precesses around fixed $\mathbf{R} = \hat{\mathbf{\Omega}}_e$ at a variable rate, and $\mathbf{S} \cdot \hat{\mathbf{\Omega}}_e$ is conserved. However, the equation of motion studied in Section IV [Eq. (35)] neglects nutation yet provides a good description of the evolution of $\bar{\theta}_e$. For the fiducial LK-induced merger, Fig. 6 shows that $\mathbf{\Omega}_e$ nutates substantially within a LK period when $\mathcal{A} \simeq 1$ (nutation is equivalent to

$\Omega_{e1} \neq 0$ and $\Delta I_{e1} \neq 0^\circ$). We infer that, even when $\mathbf{\Omega}_e$ does nutate appreciably, there are conditions for which its nutation negligibly affects $\bar{\theta}_e$ conservation.

In the main text, Section V showed that being close to a resonance $\bar{\Omega}_e \approx N\Omega_{\text{LK}}$ results in non-conservation of $\bar{\theta}_e$. However, the converse is not obviously true: our approximate analysis does not prove that being far from these resonances guarantees good conservation of $\bar{\theta}_e$. In the next section, we argue that, for the dynamics studied in this paper, this converse is likely true as well.

2. With Nutation

When $\mathbf{\Omega}_e$ is allowed to nutate within T_{LK} , the quantity given by Eq. (A2) is no longer conserved, as

$$\frac{d}{dt} [e^{-\Phi}\mathbf{S}] = e^{-\Phi} \frac{d\mathbf{S}}{dt} - \tilde{\mathbf{A}} e^{-\Phi}\mathbf{S} \neq e^{-\Phi} \left[\frac{d\mathbf{S}}{dt} - \tilde{\mathbf{A}}\mathbf{S} \right] = 0. \quad (\text{A6})$$

Instead, we define new quantities Φ' and $\tilde{\mathbf{B}}$ defined such that

$$\Phi'(t) \equiv \int_0^t \tilde{\mathbf{A}} + \tilde{\mathbf{B}} dt, \quad (\text{A7})$$

$$\frac{d}{dt} [e^{-\Phi'}\mathbf{S}] = 0. \quad (\text{A8})$$

This requires

$$\tilde{\mathbf{B}} = [e^{-\Phi'}, \tilde{\mathbf{A}}] e^{\Phi'}, \quad (\text{A9})$$

where the square brackets denote the commutator. The monodromy matrix is then

$$\tilde{\mathbf{M}} = \exp \left[\int_0^{T_{\text{LK}}} \tilde{\mathbf{A}} + \tilde{\mathbf{B}} dt \right]. \quad (\text{A10})$$

We next want to understand when Eq. (A10) can be well approximated by Eq. (A5). We first expand the matrix exponential using the Zassenhaus formula [the inverse of the well-known Baker-Campbell-Hausdorff formula, see e.g. 54]

$$\tilde{\mathbf{M}} = e^{T_{\text{LK}}\bar{\tilde{\mathbf{A}}}} e^{T_{\text{LK}}\bar{\tilde{\mathbf{B}}}} \exp \left[-\frac{T_{\text{LK}}^2 [\bar{\tilde{\mathbf{A}}}, \bar{\tilde{\mathbf{B}}}]}{2} + \dots \right]. \quad (\text{A11})$$

Note that $\tilde{\mathbf{M}}$ is a rotation matrix (see Section III A), and $\exp [T_{\text{LK}}\bar{\tilde{\mathbf{A}}}]$ is also a rotation matrix ($\tilde{\mathbf{A}}$ is skew-symmetric), so the remainder of the right-hand side above must also be a rotation matrix (as the rotation matrices are closed under matrix multiplication). For convenience, define

$$\tilde{\mathbf{R}}_A \equiv e^{T_{\text{LK}}\bar{\tilde{\mathbf{A}}}} \quad \tilde{\mathbf{R}}_B \equiv e^{T_{\text{LK}}\bar{\tilde{\mathbf{B}}}} \exp \left[-\frac{T_{\text{LK}}^2 [\bar{\tilde{\mathbf{A}}}, \bar{\tilde{\mathbf{B}}}]}{2} + \dots \right], \quad (\text{A12})$$

where $\tilde{\mathbf{R}}_A$ and $\tilde{\mathbf{R}}_B$ are rotation matrices that effect rotations by angles θ_A and θ_B about their respective axes.

When can $\tilde{\mathbf{R}}_B$ be neglected? From Eq. (A9), we see that $\tilde{\mathbf{B}} = 0$ vanishes ($\theta_B = 0$) when $[\tilde{\mathbf{A}}, \Phi]$ commute, which occurs when Ω_e does not nutate, and we recover Eq. (A5). In fact, we will argue later that θ_B is generally small for the spin dynamics studied in the main text. However, a small θ_B alone is not sufficient to assume $\tilde{\mathbf{M}} \approx \tilde{\mathbf{R}}_A$. To see this, note if θ_B is small, then $\tilde{\mathbf{R}}_B \approx \mathbf{1}$ where $\mathbf{1}$ is the 3×3 identity matrix. On the other hand, $\theta_A = \bar{\Omega}_e T_{LK}$. Then, if θ_A is not too near an integer multiple of 2π , $\tilde{\mathbf{M}} \approx \tilde{\mathbf{R}}_A$ and $\tilde{\mathbf{M}} \approx \tilde{\mathbf{R}}_A$ as before. However, if $\bar{\Omega}_e T_{LK} \approx 2\pi M$ for integer M , then $\tilde{\mathbf{R}}_A$ itself is near the identity as well, and $\tilde{\mathbf{R}}_B$ *cannot* be neglected when calculating $\tilde{\mathbf{M}}$. The criterion for neglecting $\tilde{\mathbf{R}}_B$ is then clear: θ_B must be much closer to an integer multiple of $2\pi M$ than θ_A .

To complete this picture, we argue that, for the spin dynamics studied in the main text, θ_B is small, so generally $\tilde{\mathbf{R}}_B \approx \mathbf{1}$, and $\Omega_e \approx M\Omega_{LK}$ is a *necessary* condition for \mathbf{R} to differ significantly from $\hat{\Omega}_e$. To do this, we recall that $\bar{\Omega}_e T_{LK} \lesssim 2\pi$ (Figs. 10 and 12), and we seek to show that θ_B must generally be small compared to θ_A , which would imply $\theta_B \ll 2\pi$. We first approximate that $e^{\Phi'} \approx e^\Phi$ in Eq. (A9) (requiring $\theta_B \ll \theta_A$, which we will verify retroactively, and being far from resonance, $\theta_A \neq 2\pi$), which gives

$$\tilde{\mathbf{B}} \approx [e^{-\Phi}, \tilde{\mathbf{A}}] e^\Phi. \quad (\text{A13})$$

Next, recall that Φ is the integral of $-\tilde{\mathbf{A}}$, and so the magnitude of $\tilde{\mathbf{B}}$ [$\tilde{\mathbf{B}}$ primarily affects $\tilde{\mathbf{M}}$ via its average, see Eq. (A10)] depends on the average misalignment between the vectors Ω_e and $\int' \Omega_e dt \approx \bar{\Omega}_e$. There are a few possible regimes to consider: (i) if $\mathcal{A} \gg 1$, then LK oscillations are frozen, and Ω_e does not nutate; (ii) if $\mathcal{A} \ll 1$, then $\hat{\Omega}_e \approx \hat{\mathbf{L}}_{\text{tot}} \approx \hat{\Omega}_e$ for almost all of T_{LK} ; and (iii) if $\mathcal{A} \approx 1$, then e_{max} cannot be too large [Eq. (18)], and so Ω_L and Ω_{SL} cannot vary too much within an LK cycle and the nutation of Ω_e is limited. This analysis suggests that, at least far from resonance, the nutation of Ω_e is limited, and the commutator in Eq. (A13) is small in the sense that $\theta_B \ll \theta_A$, justifying our earlier claim. While this analysis is not rigorous, it suggests that the only resonances present in the system are near $\bar{\Omega}_e = M\Omega_{LK}$ and that otherwise $\mathbf{R} \parallel \bar{\Omega}_e$, in agreement with the results of the main text.

3. Quantitative Effect

Above, we have given a qualitative analysis of the exact solution for the monodromy matrix $\tilde{\mathbf{M}}$. In this section, we aim to reconcile this with the quantitative, approximate results in the text and suggest that the results in the text constitute a complete characterization of the spin dynamics.

In Section V, we found that one effect of the $N \geq 1$ Fourier harmonics are fluctuations in $\bar{\theta}_e$ when $\bar{\Omega}_e \approx M\Omega_{LK}$ with amplitude given by Eq. (81). On the other hand, in Appendix A 2, we found that \mathbf{R} is aligned with $\bar{\Omega}_e$ except when $\bar{\Omega}_e$ is sufficiently

close to $M\Omega_{LK}$ that the nutation of Ω_e becomes important, but we were not able to determine a closed-form expression for

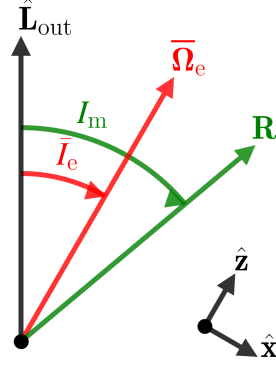


FIG. 16. Definition of angles for numerical study of the monodromy matrix rotation axis. \mathbf{R} is the eigenvector of the monodromy matrix $\tilde{\mathbf{M}}$ with eigenvalue 1.

the misalignment. In this section, we show numerically that the formulas given in the main text give good predictions for the orientation of \mathbf{R} .

To validate the analytic prediction given by Eq. (81), we numerically compute $\tilde{\mathbf{M}}$. We study the $\eta \neq 0$, LK-enhanced regime ($m_1 = m_2 = m_3 = 30M_\odot$, $a_0 = 0.1$ AU, $e_0 = 10^{-3}$, $\tilde{a}_{\text{out}} = 3$ AU). We still neglect GW dissipation in order for Floquet analysis to be applicable. For 2000 different I_0 of the inner binary, we construct $\tilde{\mathbf{M}}$ by evolving the spin equation of motion Eq. (22) starting with the three initial conditions $\mathbf{S}_0 = \hat{\mathbf{x}}$, $\mathbf{S}_0 = \hat{\mathbf{y}}$, and $\mathbf{S}_0 = \hat{\mathbf{z}}$ (see Fig. 16) over a single LK period, then using

$$\tilde{\mathbf{M}} = \Phi(T_{LK}) \Phi^{-1}(0) = \Phi(T_{LK}), \quad (\text{A14})$$

where $\Phi(t)$ is the *principal fundamental matrix solution* whose columns are solutions to Eq. (22) and $\Phi(0)$ is the identity. \mathbf{R} is then the eigenvector that has eigenvalue 1. Note that if \mathbf{v} is an eigenvector, so too is $-\mathbf{v}$; we choose convention that \mathbf{R} points in the same direction as $\bar{\Omega}_e$, i.e. $\Delta I_m \equiv |I_m - \bar{I}_e| < 90^\circ$.

The orientation of \mathbf{R} is related to the $|\Delta\bar{\theta}_e|$ predicted by Eq. (81): if \mathbf{R} and $\bar{\Omega}_e$ are misaligned by angle ΔI_m , then $\bar{\theta}_e$ oscillates with semi-amplitude ΔI_m . Thus, we can infer ΔI_m in the vicinity of each $\bar{\Omega}_e = M\Omega_{LK}$ resonance from Eq. (81), and we obtain by linearity that

$$\Delta I_m \sim \sum_{M=1}^{\infty} \frac{d(M)}{2} \left| \frac{\Omega_{eM} \sin \Delta I_{eM}}{\bar{\Omega}_e - M\Omega_{LK}} \right|. \quad (\text{A15})$$

Fig. 17 shows that this calculation predicts the numeric ΔI_m well. In particular, the amplitude of both resonances are well predicted, suggesting that the approximate factor $d(M)$ introduced in Eq. (81) is accurate. This supports our assertion that \mathbf{R} deviates from $\bar{\Omega}_e$ at resonances $\bar{\Omega}_e \approx M\Omega_{LK}$, and the misalignment is captured by Eq. (81).

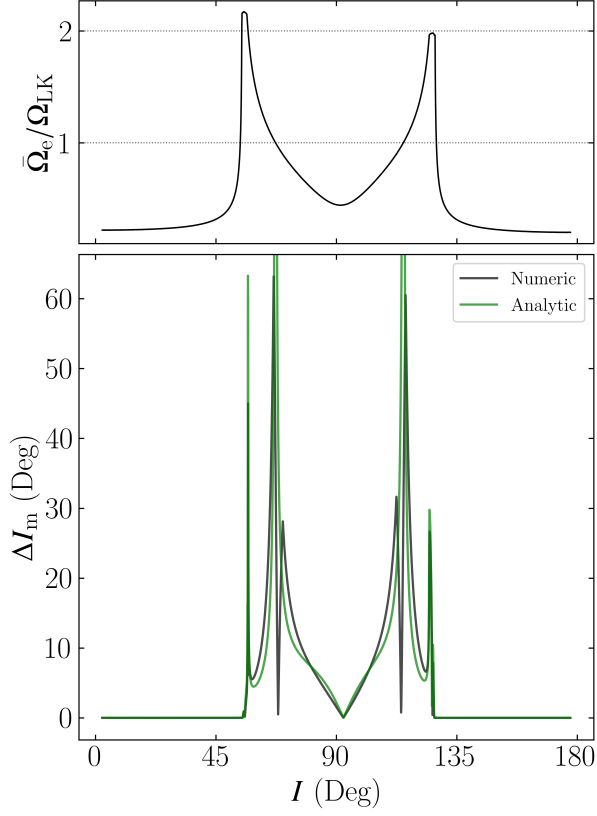


FIG. 17. Comparison of the orientation \mathbf{R} obtained from numerical simulations of Eq. (22) in the $\eta \neq 0$, LK-enhanced parameter regime ($m_1 = m_2 = m_3 = 30M_\odot$, $a_0 = 0.1$ AU, $e_0 = 10^{-3}$, $\tilde{a}_{\text{out}} = 3$ AU) with the analytic resonance formula given by Eq. (A15) as a function of initial inclination, in the absence of GW dissipation. The top panel shows the ratio $\bar{\Omega}_e / \Omega_{LK}$ is shown as the solid black line, while the horizontal dashed lines denote $\bar{\Omega}_e = \Omega_{LK}$ and $\bar{\Omega}_e = 2\Omega_{LK}$. The bottom panel shows the misalignment angle between the numerically-computed \mathbf{R} and $\bar{\Omega}_e$ as the black line. Separately, the predicted misalignment ΔI_m due to interaction with the Fourier harmonics is given by Eq. (A15). We see that the scaling of the misalignment angle near resonances is well captured by our analytic formula, but the numerical misalignment angle crosses 0 within the $M = 1$ resonance, which is not predicted by our simple theory.